Materials for Renewable and Sustainable Energy (2026) 15:40
https://doi.org/10.1007/s40243-026-00378-2

ORIGINAL PAPER

Non-stoichiometric Mg-Ni composites for hydrogen storage: role of in-situ Mg_2Ni formation in enhancing hydrogen sorption performance

Babak O'. Shahreza[1,2,3] · Julia Ivanisenko[4] · Fjodor Sergejev[3] · Hosseinali Omranpour[5] · Jacques Huot[1]

Received: 13 October 2025 / Accepted: 4 May 2026

Abstract

Magnesium-based alloys are promising hydrogen storage materials due to their high capacity but suffer from slow hydrogenation kinetics and high operating temperatures. While high-pressure torsion (HPT) enhances kinetics through microstructural refinement, and nickel addition provides catalytic effects, their combined influence on hydrogen storage performance remains insufficiently characterized. This work investigates Mg-Ni composites with variable Ni content (2–16 at%). After consolidating the powders by HPT and activating them in a Sievert apparatus, in-situ differential scanning calorimetry (DSC) was used to track phase evolution and extract thermodynamic parameters. DSC thermal cycling under hydrogen promoted the in-situ solid-state synthesis of Mg_2Ni from the elemental mixtures. Activation energy analysis revealed systematic reduction with increasing Ni content. While HPT enhanced initial hydrogenation kinetics, thermodynamic parameters (enthalpy, entropy) showed no systematic variation across HPT conditions, as high thermal cycling temperatures (up to 450 °C) led to the annealing of HPT-induced structural defects. The findings demonstrate that compositional tuning through in-situ Mg_2Ni formation dominates hydrogen storage performance, with HPT serving primarily as an initial activation aid.

Keywords Severe plastic deformation · Metal hydrides · In-situ phase transformation · Hydrogen sorption · Thermodynamic hysteresis

Introduction

Magnesium and its alloys are among the most promising candidates for solid-state hydrogen storage due to their lightweight, high hydrogen storage capacity, and relatively low cost [1]. Pure magnesium can retain hydrogen up to 7.6 wt%, which is the highest capacity among all recognized metal hydrides reported to date [2, 3]. However, its practical application is hindered by slow hydrogen absorption and desorption kinetics, as well as the need for high temperatures to achieve reasonable hydrogenation rates [4].

To overcome the slow hydrogenation kinetics in magnesium hydride, two complementary strategies have been developed: catalytic alloying and mechanical nanostructuring [1, 5, 6]. Catalytic additives, particularly transition metals such as Ni, Co, and Fe, enhance hydrogen storage performance through multiple mechanisms. First, they facilitate the dissociation and recombination of H_2 molecules at the material surface, accelerating the rate-limiting step [7–9]. Second, certain elements can form intermetallic phases with different thermodynamic properties and crystal

✉ Babak O'. Shahreza
babakomr@ucm.es

1 Hydrogen Research Institute, University of Quebec in Trois-Rivieres (UQTR), 3351 Des Forges, Trois-Rivieres G9A 5H7, Canada

2 Department of Chemical and Materials Engineering, Complutense University of Madrid (UCM), Av. Complutense, 28040 Madrid, Spain

3 Department of Mechanical and Industrial Engineering, Tallinn University of Technology (TalTech), Ehitajate Tee 5, 19086 Tallinn, Estonia

4 Institute of Nanotechnology (INT), Karlsruhe Institute of Technology (KIT), 76021 Karlsruhe, Germany

5 Department of Mechanical and Industrial Engineering, University of Toronto, 5 King's College Road, Toronto, ON M5S 3G8, Canada

Published online: 26 June 2026

structures that may provide more favorable hydrogen diffusion pathways [10]. For instance, nickel in magnesium systems promotes the formation of *Mg_2Ni*, which subsequently enables the formation of Mg_2NiH_4—a hydride with lower decomposition temperature and enhanced kinetics compared to MgH_2 [11, 12]. The catalytic effect thus operates through both surface activation and bulk phase modification.

Complementary to catalytic approaches, severe plastic deformation (SPD) techniques enhance hydrogenation kinetics by mechanical nanostructuring effects without altering composition [6, 13]. SPD methods, particularly High-Pressure Torsion (HPT), reduce grain sizes to the nanometer scale and introduce high densities of dislocations and stacking faults [14–16]. These structural features serve dual roles: grain boundaries and stacking faults provide high-diffusivity pathways for hydrogen penetration [17, 18], while dislocations act as nucleation sites for hydride formation [19]. HPT produces nanostructures comparable to advanced composite materials such as nanostructured aerogel fibers, where controlled hierarchical architectures enable exceptional property combinations [20]. While catalytic alloying and HPT processing have each been extensively studied for improving Mg-based hydrogen storage, their combined and relative contributions within a unified design framework have received less systematic attention [21, 22]. A critical knowledge gap exists regarding their competitive or synergistic interaction. It is currently unclear whether the high defect density from HPT remains the primary kinetic driver after the first thermal cycle, or if the in-situ formation of intermetallic phases like *Mg_2Ni* overrides the initial microstructural refinement. Without decoupling these effects, the physical origin of the kinetic enhancement remains unclear. Furthermore, a methodological gap exists in the synthesis of these composites. Previous studies on Mg-Ni systems have primarily focused on stoichiometric compositions, particularly pre-alloyed Mg_2Ni and its hydride Mg_2NiH_4 [11, 23]. However, the behavior of non-stoichiometric Mg-Ni composites under combined HPT processing and in-situ phase evolution during hydrogen cycling has been relatively unexplored [19, 21]. Understanding how in-situ phase evolution during hydrogen storage cycling affects performance could provide valuable insights for practical material design, where perfect stoichiometry may not be guaranteed. Moreover, identifying the dominant factor -compositional tuning versus microstructural refinement- can guide more cost-effective processing strategies [22, 24, 25].

Although Pressure-Composition-Temperature (PCT) measurements yield established equilibrium thermodynamics, characterization of HPT-processed materials presents practical challenges due to their small sample quantities (typically 5–20 mg extracted from a single disk) [21, 26].

In-situ differential scanning calorimetry (DSC) experiments offer a synergistic alternative for such materials, enabling quantitative thermodynamic and kinetic analyses from milligram-scale samples alongside real-time observation of solid-state phase transformations during thermal cycling [27, 28]. Even though previous DSC studies of SPD-processed hydrides have primarily provided qualitative assessments [14, 29–32], there is a need for systematic quantitative analysis to correlate compositional tuning with the resulting sorption behavior.

The present study investigates Mg-Ni composites with variable Ni content (2–16 at%) processed by HPT, with the objectives of: (1) quantifying the relative contributions of composition versus microstructural refinement to hydrogen storage performance; (2) characterizing in-situ phase evolution during hydrogen cycling, utilizing the DSC as a mini-reactor for the solid-state synthesis of Mg_2Ni from non-stoichiometric elemental mixtures. By leveraging this *in-situ* approach, we bypass the requirement for traditional pre-alloying steps (such as ball milling [33]), providing a facile route to evaluate the storage behavior of materials. The combined use of Sievert apparatus measurements, *in-situ* DSC, and post-cycling XRD enables a comprehensive assessment of both the initial activation and the following cycling performance.

Materials and methodology

Magnesium (Mg) powder with a mesh size of 100–200 and a purity of 99.6%, provided by ThermoFisher, and Nickel (Ni) powder with a purity of 99.99% and a mesh size of 100, purchased from MaTeck, were used for composition preparation. To study the catalytic effect of Ni on the hydrogenation of Mg, four different compositions were prepared: Mg with 2, 4, 6, and 16% Ni, all in atomic percentages (sample codes are provided in Table 1). The compositions were weighed and prepared in a glovebox under an argon atmosphere. Pre-compaction and HPT processing were performed in air at room temperature. Each sample was subjected to pre-compaction at 566 MPa and then, HPT processing at 5 GPa. Each sample weighed between 0.2 and 0.26 g, and the sample diameter was ~ 1 cm. The samples underwent 1 and 5 full rotations during HPT processing. One sample (MgNi16-N0) in the pre-compacted state without any HPT turns was also prepared as a reference. The HPT facility was computer-controlled to ensure precise monitoring of rotation numbers. Microhardness testing was conducted by a Micro Vickers Hardness Tester model 900–391. Hydrogenation of the samples was carried out in a homemade Sievert-type apparatus with calibrated volumes at 300 °C and under a hydrogen atmosphere with a pressure

Table 1 Sample codes and Vickers microhardness values measured at the center (r = 0 mm) and edge (r ≈ 4.6 mm) of the disks

Sample code*	Ni content (at%)	Number of HPT turns (N)	Center	Edge
MgNi2	2	N = 1	39 (2)	45 (3)
		N = 5	39 (3)	48 (4)
MgNi4	4	N = 1	43 (2)	54 (3)
		N = 5	42 (3)	59 (4)
MgNi6	6	N = 1	54 (2)	62 (2)
		N = 5	55 (2)	68 (3)
MgNi16	16	N = 0	55 (2)	54 (2)
		N = 1	61 (2)	71 (4)
		N = 5	63 (3)	80 (4)

The numbers in the parentheses represent the marginal error of the last significant digit

*Hereinafter, the samples are presented as MgNia-Nb, where "a" represents the atomic percentage of Ni and "b", the number of HPT turns, such as MgNi2-N5

of 30 bar. The HPT-processed disks were cut into small fragments of approximately 2–4 mm and subsequently placed in the Sievert reactor for hydrogenation. Microstructural observations of the sample and chemical analysis were conducted using a Hitachi SU1510 scanning electron microscope (SEM) equipped with an EDX (energy-dispersive X-ray) apparatus from Oxford Instruments. A Bruker D8 Focus obtained the x-ray diffraction (XRD) patterns with Cu Kα radiation (λ = 1.5406 Å), and the Topas software (ver. 7) performed the Rietveld refinement of the patterns [34]. XRD analysis was performed on samples before hydrogenation, after hydrogenation in the Sievert apparatus, and after DSC cycling to track phase evolution. DSC measurements were performed using a TA Instruments DSC-25P apparatus capable of operating under controlled gas atmospheres and pressures. Sample masses ranged from 15 to 25 mg, obtained by fragmenting the hydrogenated chunks. For ex-situ dehydrogenation, hydrogenated samples were first dehydrogenated under an argon atmosphere at 3 bar absolute pressure to characterize the as-prepared hydride phases. For kinetic evaluation via the Kissinger method, separate dehydrogenation runs were conducted at heating rates of 2, 5, 10, and 20 $K \cdot min^{-1}$ to determine the activation energy (E_a).

For in-situ cycling, following the initial dehydrogenation, samples were subjected to in-situ hydrogenation and dehydrogenation cycles under a hydrogen atmosphere at three different absolute pressures of 6, 11, and 21 bar (5, 10, and 20 bar gauge pressure). These measurements were performed at a constant heating/cooling rate of 2 $K \cdot min^{-1}$ to approximate near-equilibrium conditions and minimize kinetic effects, as faster rates introduce systematic kinetic artifacts that shift peak temperatures away from true equilibrium values.

Results

Microstructure and hardness evolution

Microhardness testing was applied to the surface of the HPT-processed samples to assess the impact of HPT on the mechanical behavior of the material. Indentations were applied to the Mg-rich matrix regions, avoiding nickel particles, to assess the deformation response of the dominant phase. The results are shown in Table 1. This table shows that the two factors, the number of turns in HPT, and the nickel content, are the influential parameters increasing the hardness of the material. However, the central zone of the sample (r ≈ 0 mm) is essentially insensitive to the number of turns. This behavior is consistent with the HPT strain field: shear strain increases with radial position, so sample regions farther from the disk center experience higher imposed strain and correspondingly larger hardness increases [35]. Additionally, the effect of nickel content is pronounced at the edge (r ≈ 4.6 mm), where hardness increases by up to ~ 67% for MgNi16 compared with MgNi2.

Earlier studies on the Mg-Ni alloy can confirm these findings, where increasing Ni content corresponded to enhanced hardness [36–38]. However, the hardness values observed in this work are slightly lower, ranging from 45 to 80 HV, which is typically 10–20 HV below the reported values. This discrepancy is understandable since, in earlier works, Mg turnings were melted with Ni particles, enhancing the homogeneity [36], and the presence of a secondary phase strengthened the composition [37].

X-ray diffraction (XRD) analysis was performed on samples before hydrogenation to evaluate microstructural changes induced by HPT. Figure 1 presents the XRD patterns of the as-received and HPT-processed samples before hydrogenation.

Except for MgNi16-N0, which was only compacted, all other samples that experienced HPT, showed preferred orientations. Rietveld refinement of the patterns revealed the crystallite size and the amount of microstrain imposed on the samples, shown in Table 2.

Hydrogen storage behavior

First hydrogenation kinetics

Figure 2 shows the hydrogen uptake curves during the first hydrogenation cycle (activation at 30 bar and 300 °C for 24 h). In addition to the microstructural refinement by HPT, first hydrogenation kinetics demonstrated a strong compositional dependence on Ni content. MgNi2 and MgNi4 samples exhibited sluggish uptake, reaching only ~ 0.7 wt% within 24 h regardless of HPT turns, indicating insufficient

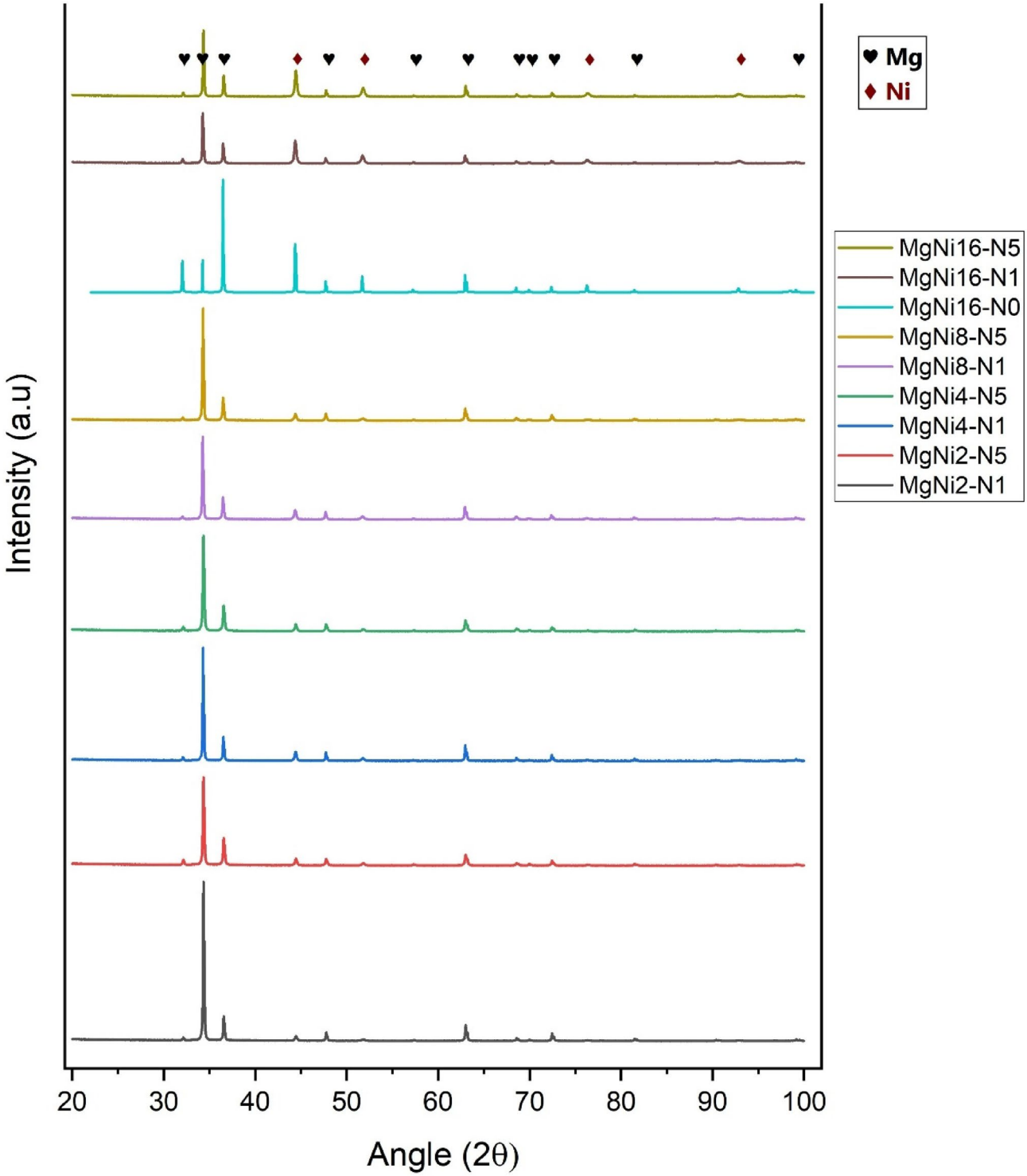

Fig. 1 XRD patterns of the as-received HPT samples -before hydrogenation

Ni content for effective catalysis. A remarkable kinetic transition occurred at 6 at% Ni: MgNi6-N5 achieved 1.5 wt% in 24 h, representing a more than twofold improvement over lower Ni compositions. The MgNi16 series showed the fastest kinetics, with MgNi16-N5 reaching 3.3 wt% within 24 h, nearly fourfold enhancement compared to MgNi2 and MgNi4 samples. Such behavior indicates that HPT provides a modest but measurable enhancement: MgNi16-N0 (no HPT turns) reached ~ 2.8 wt% while MgNi16-N5 (five HPT turns) achieved 3.3 wt%. The improvement is attributed to

Table 2 Structural information of samples before hydrogenation

Composition	Number of HPT rotations	Structure	Crystallite size (nm)	Micro-strain (%)
MgNi2	1	Mg	90(1)	0.010(8)
		Ni	125(13)	0.019(8)
	5	Mg	66(1)	0.031(1)
		Ni	79(1)	0.095(6)
MgNi4	1	Mg	107(1)	0.014(1)
		Ni	64(6)	0.096(4)
	5	Mg	64(1)	0.031(1)
		Ni	62(7)	0.079(6)
MgNi6	1	Mg	81 (1)	0.013 (1)
		Ni	57 (5)	0.094 (4)
	5	Mg	90 (2)	0.035 (1)
		Ni	57 (7)	0.093 (7)
MgNi16	1	Mg	91(2)	0.013 (2)
		Ni	45 (1)	0.075 (2)
	5	Mg	79 (1)	0.010 (2)
		Ni	48 (2)	0.079 (2)
	0	Mg	142 (14)	–
		Ni	202 (38)	0.010 (1)

The numbers in parentheses show the error for the last significant digit

grain refinement and defect introduction, which create diffusion pathways facilitating hydrogenation [13], especially when sufficient Ni is present to catalyze H_2 dissociation. These results show that compositional tuning (Ni addition) is the dominant driver of kinetic performance, while mechanical nanostructuring enhances kinetics synergistically in Ni-rich compositions, particularly during the first activation cycle [19, 39].

To provide deeper insight into the catalytic influence of Ni and mechanical nanostructuring, we performed a kinetic rate analysis of the initial hydrogenation. The motivation for this analysis is first, to decouple the mechanical effect of HPT-induced defect density from the chemical effect of Ni-induced catalytic sites; and second, to compare the kinetic rates during the challenging first activation cycle.

To quantify these kinetics, the hydrogen uptake data were converted into the extent of reaction, α, defined as:

$$\alpha = \frac{H_t}{H_{Max}} \tag{1}$$

where H_t is the hydrogen content absorbed at time t, and H_{Max} is the theoretical capacity of the Mg-matrix (accounting for the weight fraction of Ni as non-storing content). This normalization enables a direct comparison of sorption kinetics across different compositions.

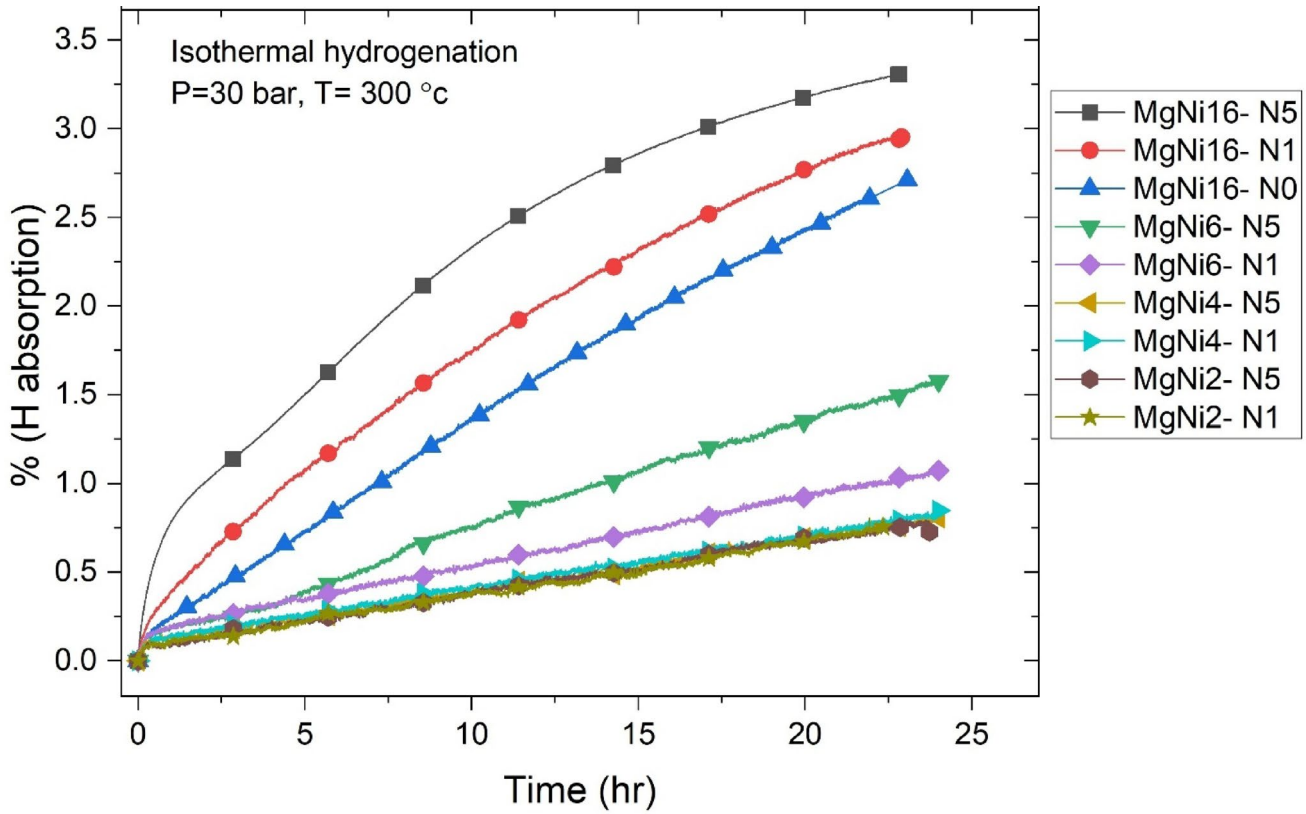

Fig. 2 Hydrogenation kinetics of samples in the Sievert apparatus

Table 3 Hydrogen uptake and extent of reaction (α) during the first hydrogenation at 300 °C and 30 bar H_2 pressure

Reaction Time		2 h	12 h	24 h
MgNi2-N1	H uptake (wt%)	0.13	0.43	0.76
	Extent of reaction (α)	**0.02**	**0.06**	**0.10**
MgNi2-N5	H uptake (wt%)	0.13	0.45	0.80
	Extent of reaction (α)	**0.02**	**0.06**	**0.11**
MgNi4-N1	H uptake (wt%)	0.15	0.48	0.83
	Extent of reaction (α)	**0.02**	**0.07**	**0.12**
MgNi4-N5	H uptake (wt%)	0.15	0.47	0.85
	Extent of reaction (α)	**0.02**	**0.07**	**0.12**
MgNi6-N1	H uptake (wt%)	0.22	0.61	1.09
	Extent of reaction (α)	**0.03**	**0.09**	**0.16**
	H uptake (wt%)	0.23	0.88	1.59
MgNi6-N5	**Extent of reaction (α)**	**0.03**	**0.13**	**0.24**
	H uptake (wt%)	0.37	1.61	2.71
MgNi16-N0	**Extent of reaction (α)**	**0.07**	**0.31**	**0.52**
	H uptake (wt%)	0.58	1.99	2.96
MgNi16-N1	**Extent of reaction (α)**	**0.11**	**0.38**	**0.56**
	H uptake (wt%)	1.00	2.57	3.31
MgNi16-N5	**Extent of reaction (α)**	**0.19**	**0.49**	**0.63**

The values for the extent of reaction (alpha) represent a normalized, dimensionless fraction calculated directly from the experimental hydrogen uptake divided by the fixed theoretical maximum capacity(H_t/H_{max}). The values are reported to two decimal places to reflect the physical significance and precision limits of the volumetric measurement system, and as a normalized ratio, they do not carry independent experimental error margin

The kinetics were assessed by comparing **α** at key time intervals (t = 2h, 12h, 24h), as summarized in Table 3. Figure 3 illustrates the α values versus time profiles, revealing the kinetic evolution and catalytic impact of Ni addition. The results reveal a kinetic transition: while MgNi2 and MgNi4 samples exhibit sluggish kinetics, reaching only α ≈ 0.10 within 24 h, the MgNi16-N5 composition achieves α = 0.63 in the same timeframe, representing a 6.3-fold enhancement over the low-Ni samples. The data indicate that while mechanical nanostructuring via HPT provides a measurable enhancement, compositional tuning via Ni addition acts as the dominant kinetic driver. Specifically, the higher density of Ni-rich interfaces in the MgNi16 series facilitates hydrogen dissociation, effectively lowering the barrier for hydride nucleation. A notable synergistic effect is observed in the MgNi16 series, where HPT processing (N5) increased the extent of reaction (α) from 0.52 (N0) to 0.63 (N5) at the 24-h mark, a 21% relative improvement. As shown in Fig. 3, all samples exhibit a linear progression throughout the 24-h period except for the MgNi16 series, which displays a steeper initial slope, indicating an accelerated hydrogen uptake from the onset of the reaction. This suggests that the grain refinement and defect density provided by HPT most effectively enhance hydrogen transport when a sufficient threshold of catalytic Ni sites is present. In contrast, the low-Ni compositions (2 and 4 at%) remained kinetically limited regardless of HPT turns, failing to reach even 15% of their theoretical capacity within 24 h.

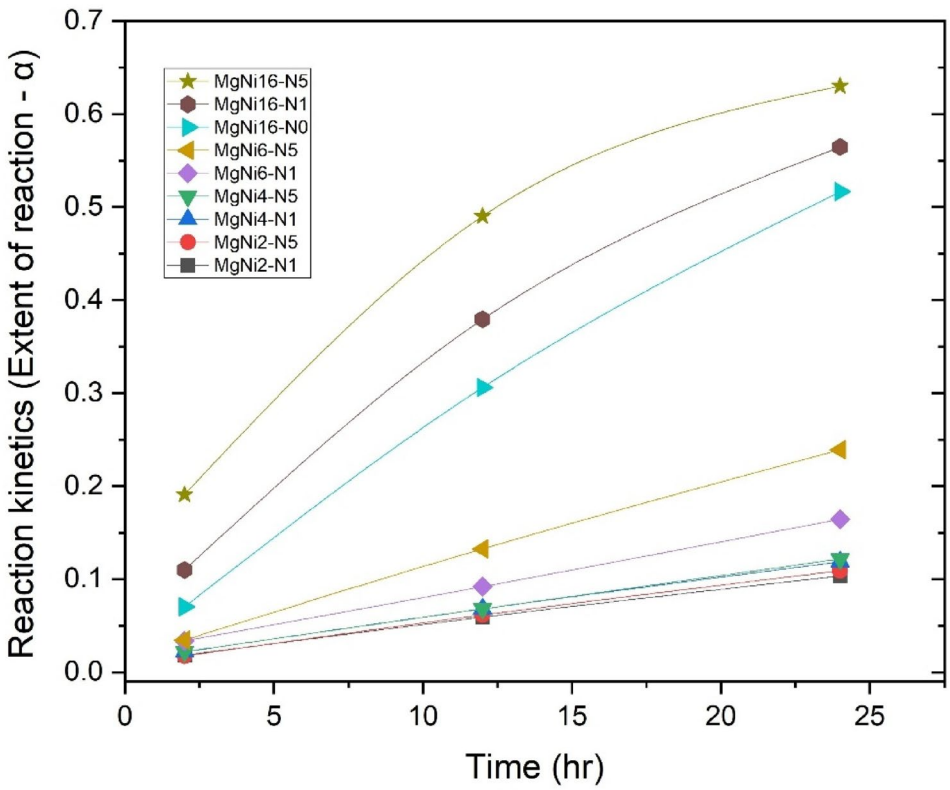

Fig. 3 Extent of reaction (α) as a function of time for Mg-Ni composites during first hydrogenation

Table 4 Activation energy values for dehydrogenation determined by the Kissinger method under an argon atmosphere

Sample ID	Activation energy E_a (kJ·mol^{-1})		
	HPT turns		
	0	1	5
MgNi2	–	181 ± 14	175 ± 13
MgNi4	–	176 ± 13	166 ± 13
MgNi6	–	169 ± 11	158 ± 12
MgNi16	177 ± 14	165 ± 13	156 ± 12

Error values represent standard errors from linear regression of DSC peak shifts

Activation energy analysis

To quantify the kinetic barriers to hydrogen release, activation energy (E_a) values were determined from DSC dehydrogenation experiments under an argon atmosphere using the Kissinger method [40]. Measurements were performed at multiple heating rates (β = 2, 5, 10, and 20 K·min^{-1}). This approach relates the heating rate (β) to the peak temperature (T_p) according to Eq. (2):

$$Ln\left(\frac{\beta}{T_p^2}\right) = -\frac{E_a}{RT_p} + const. \quad (2)$$

where R is the ideal gas constant (R = 8.314 J.mol^{-1}.K^{-1}), and T_p is the peak temperature corresponding to the maximum reaction rate. Assuming a linear relationship as Y = aX + b, the Kissinger plot is constructed by plotting Ln(β/T_p^2) versus $1/T_p$. The activation energy is then calculated from the slope of the resulting linear regression line E_a = —Slope × R [41].

Table 4 summarizes the activation energy values for MgH_2 dehydrogenation across all compositions and HPT conditions. The results reveal systematic trends with both Ni content and HPT processing, which are aligned with earlier reports [17, 42].

Figure 4 visualizes the trends and deviations of the activation energy with respect to the composition and HPT turns. As shown here, for samples after one HPT turn, E_a decreased from 181 ± 14 kJ·mol⁻1 (MgNi2-N1) to 165 ± 13 kJ·mol⁻1 (MgNi16-N1). After five HPT turns, a similar compositional trend was observed, with E_a ranging from 175 ± 13 kJ·mol⁻1 (MgNi2-N5) to 156 ± 12 kJ·mol⁻1 (MgNi16-N5).

These values are consistent with literature reports for MgH_2 systems, which typically range from 110 to 170 kJ·mol⁻1 depending on preparation method and catalysts [43–49]. The systematic reduction in E_a with increasing Ni content demonstrates the catalytic role of nickel in lowering the kinetic barrier for hydrogen release. HPT processing contributes an additional modest reduction, with the effect being most pronounced in higher Ni-content samples where defect-assisted diffusion can synergize with catalytic sites[21, 26].

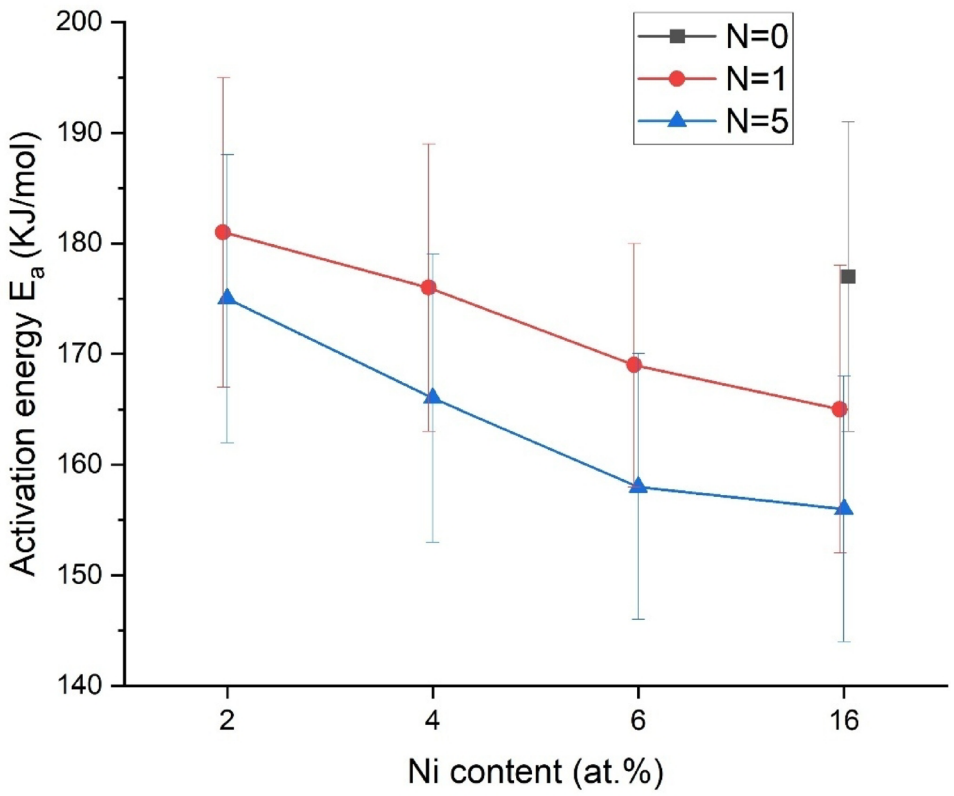

Fig. 4 Activation energy for dehydrogenation in Mg–Ni composites with respect to Ni content and HPT turns. Error bars represent standard errors from the linear regression of the Kissinger method

Phase evolution and thermodynamic analysis

Microstructural evolution after hydrogenation

Results from X-ray diffraction (XRD) analysis on the hydrogenated samples demonstrated the presence of the hydride phase (MgH_2- Fig. 5), along with unreacted magnesium and nickel. Subsequent Rietveld refinement provided quantitative data on the percentage of each phase, as well as the crystallite size and microstrain imposed on the material (Table 5).

SEM images of the hydrogenated samples revealed key microstructural details. The matrix appears as a bright gray phase, representing pure magnesium. The white regions correspond to nickel islands, and the dark gray regions indicate the hydride phase (MgH_2). The samples were only partially hydrogenated, as not all of the Mg matrix had absorbed hydrogen. As Fig. 6a to j shows, the dark regions are mainly found around the nickel islands, which provides visual evidence of the catalytic impact of nickel on the hydrogenation process. Furthermore Fig. 7 demonstrates the elemental distribution and phase morphology of the HPT-processed sample MgNi2-N1, illustrating the dispersion of Ni powder within the Mg matrix.

In-situ phase evolution during DSC cycling

Following the first hydrogenation cycle in the Sievert apparatus, samples were analyzed by Differential Scanning Calorimetry (DSC) to characterize phase transformations during hydrogen cycling. Dehydrogenation was first performed under an argon atmosphere. Thereafter, a slow heating/cooling ramp of 2 $K \cdot min^{-1}$ was applied under 21 bar hydrogen pressure up to 550 °C to promote the solid-state reaction between Mg and Ni. At these elevated temperatures, the initial decomposition of MgH_2 provides metallic magnesium, which reacts with nickel to form the Mg_2Ni intermetallic phase. Subsequently, the ternary hydride (Mg_2NiH_4) is formed during the cooling cycle under hydrogen pressure [50]. This multi-stage process can be represented as follows:

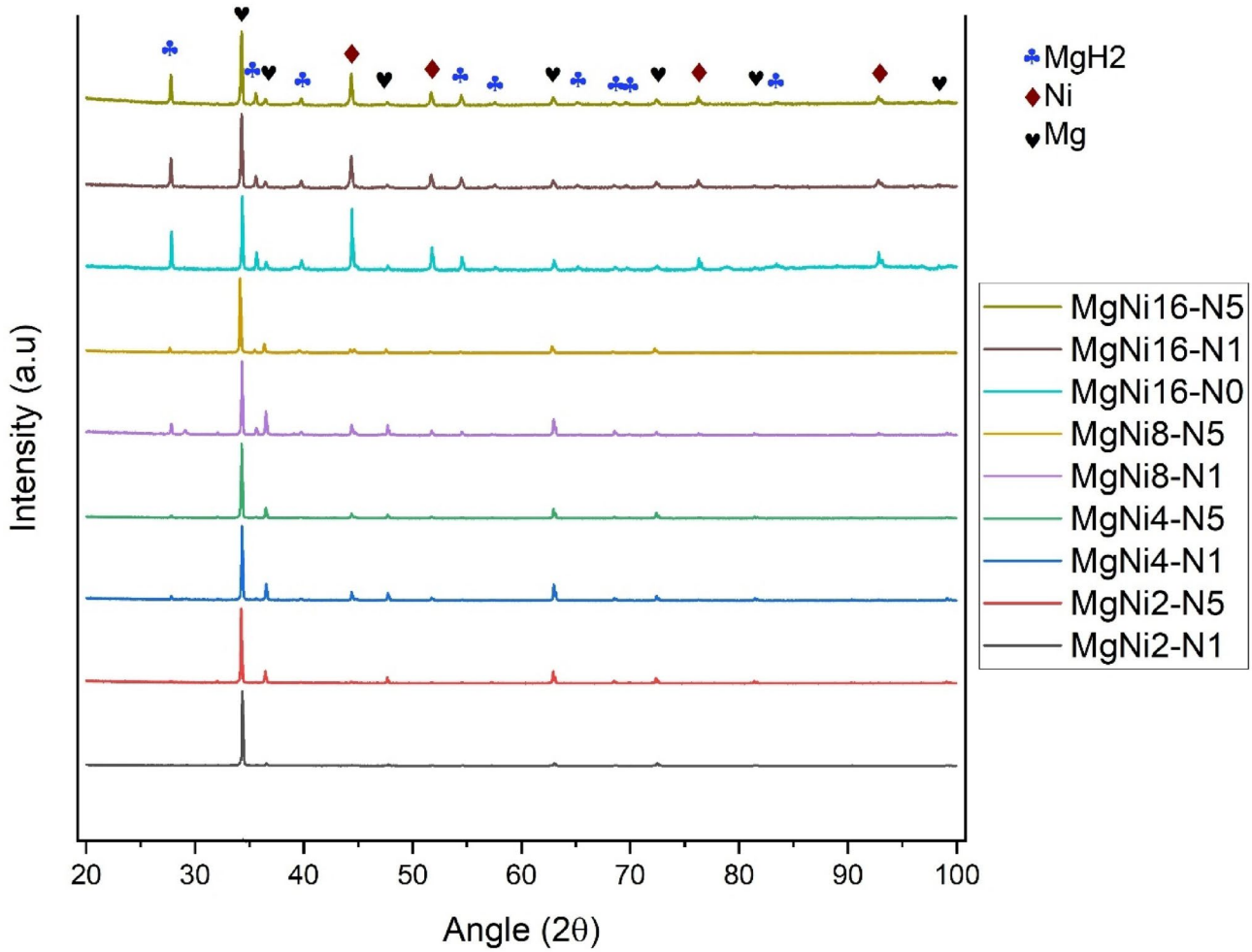

Fig. 5 XRD patterns of samples after hydrogenation

Table 5 Structural information of samples after hydrogenation

Sample	Number of HPT rotations	Structure	Percentage (wt%)	Crystallite size (nm)	Microstrain (%)
MgNi2	1	Mg	86(2)	164(3)	0.0213(7)
		MgH_2	11(2)	91(9)	–
		Ni	3.2(9)	53(19)	–
	5	Mg	91(6)	165(5)	0.0196(8)
		MgH_2	5(2)	65(10)	–
		Ni	3(1)	56(11)	–
MgNi4	1	Mg	81(5)	141(4)	0.0243(9)
		MgH_2	7(5)	121(13)	0.085(12)
		Ni	11(4)	69(7)	–
	5	Mg	82(6)	136(4)	0.0225(10)
		MgH_2	8(1)	77.8(60)	0.104(19)
		Ni	10(5)	46(5)	–
MgNi6	1	Mg	68(2)	160(8)	0.027(2)
		MgH_2	20(1)	140(30)	0.039(5)
		Ni	12(7)	69(7)	–
	5	Mg	70(1)	160(6)	0.034(2)
		MgH_2	18(1)	160(50)	0.046(7)
		Ni	12(1)	59 (6)	–
MgNi16	1	Mg	26(1)	180(20)	0.045(3)
		MgH_2	41(2)	116(11)	0.029(4)
		Ni	34(4)	99(7)	–
	5	Mg	23(4)	151(12)	0.071(2)
		MgH_2	44(3)	97(7)	0.054(3)
		Ni	33(2)	61(3)	0.026(2)
	0	Mg	24(1)	152 (11)	0.045(3)
		MgH_2	43(2)	111(23)	0.034(5)
		Ni	33(2)	62 (6)	-

The numbers in parentheses show the error for the last significant digits

$$2MgH_2 + Ni \rightarrow 2Mg + 2H_2 + Ni \rightarrow Mg_2Ni + 2H_2 \rightarrow Mg_2NiH_4 \quad (3)$$

Thereafter, the in-situ DSC measurements were carried out under a hydrogen atmosphere at three different absolute pressures of 6, 11, and 21 bar. These measurements allowed for consecutive dehydrogenation and hydrogenation cycles (Fig. 8b).

As shown in Fig. 5, the Mg_2Ni phase was not present in samples after initial hydrogenation in the Sievert apparatus. However, during subsequent in-situ DSC cycling, this intermetallic compound was formed through a solid-state reaction between elemental Mg and Ni. Once established, Mg_2Ni acted as an active phase that facilitated the subsequent hydrogenation and dehydrogenation of the Mg_2NiH_4 phase. This phase is thermodynamically less stable and decomposes and forms at lower temperatures than MgH_2 (see Fig. 8b; peaks 2 and 5). Specifically, the DSC-induced formation of Mg_2Ni lowers the kinetic barrier for both hydrogen absorption and desorption [51], serving as an effective route to create highly active sites for hydrogen storage materials [52, 53]. To confirm the presence of Mg_2Ni during DSC cycling quantitatively, X-ray diffraction analysis was performed on a MgNi16 sample after completing the DSC hydrogenation/dehydrogenation cycles under hydrogen. Rietveld refinement by Topas (Fig. 9) revealed that the sample consisted of 64 wt% Mg_2NiH_4 after hydrogenation. The dominant presence of Mg_2NiH_4 confirms that the repeated thermal cycling under hydrogen pressure induced the reaction between Mg and Ni, forming this active intermetallic phase. This structural transformation explains the emergence of low-temperature dehydrogenation peaks in DSC thermograms (Fig. 8b, Peak 2 at about 350 °C), corresponding to the decomposition of Mg_2NiH_4, which is thermodynamically less stable than MgH_2 (Peak 3 at around 390 °C). In addition to the primary sorption peaks, secondary thermal events labeled as peaks 1 and 6 in Fig. 8b were observed. These correspond to the reversible polymorphic structural transformation of the Mg_2NiH_4 phase, representing the transition between the high-temperature cubic structure ($Fm\bar{3}m$) and the low-temperature monoclinic structure (*C2/c*) [54, 55], which typically occurs around 235 °C. The substantial Mg_2NiH_4 content (64 wt%) demonstrates extensive in-situ Mg_2Ni formation during DSC cycling. The presence of MgO (14 wt%) indicates that significant Mg was consumed by oxidation during sample handling, reducing the Mg available for Mg_2Ni or MgH_2 formation.

Thermodynamic parameters via Van't Hoff analysis

Following confirmation of in-situ Mg_2Ni formation, thermodynamic analysis utilizing van't Hoff plots [56], was performed to determine the enthalpy (ΔH) and entropy (ΔS) of hydrogenation and dehydrogenation (Fig. 10). Van't Hoff analysis utilizes the relationship between equilibrium hydrogen pressure and temperature, as described by the van't Hoff equation [57]:

$$Ln\frac{P}{P_0} = -\frac{\Delta H}{R}\cdot\frac{1}{T} + \frac{\Delta S}{R} \quad (4)$$

where P is the equilibrium hydrogen pressure, P_0 is the standard state pressure, which is conventionally defined as 1 bar, ΔH is the enthalpy of dehydrogenation, ΔS is the entropy of dehydrogenation, R is the ideal gas constant (8.314 $J.mol^{-1}.K^{-1}$), and T is the absolute temperature in Kelvin [58]. DSC experiments were conducted at three different hydrogen pressures (6, 11, and 21 bar absolute). For each de/hydrogenation peak, a van't Hoff plot of Ln(P) versus 1/T was then constructed, where the slope corresponds to $-\Delta H/R$ and the intercept to $\Delta S/R$ (see Fig. 10). It should be noted that although DSC is used here as a non-isothermal calorimetric proxy for equilibrium thermodynamics, this approach follows established methodologies reported for Mg-based

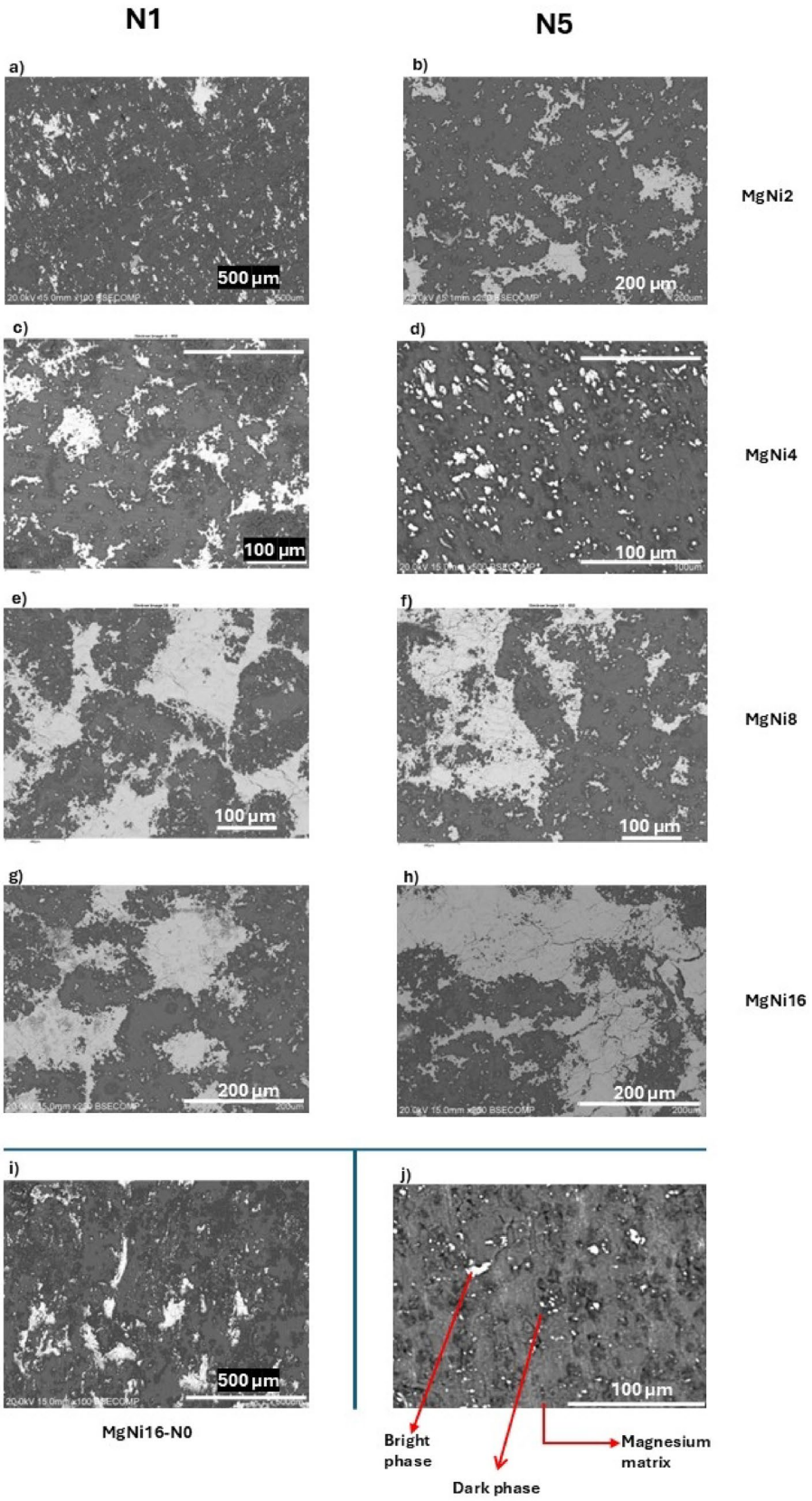

Fig. 6 SEM micrographs of Mg-Ni samples after hydrogenation. Images (**a**-**h**) show partially hydrogenated samples of different compositions after one HPT turn (**a**, **c**, **e**, and **g**) and five HPT turns (**b**, **d**, **f**, and **h**). Images (i-j) show a MgNi16 sample without HPT (N = 0)

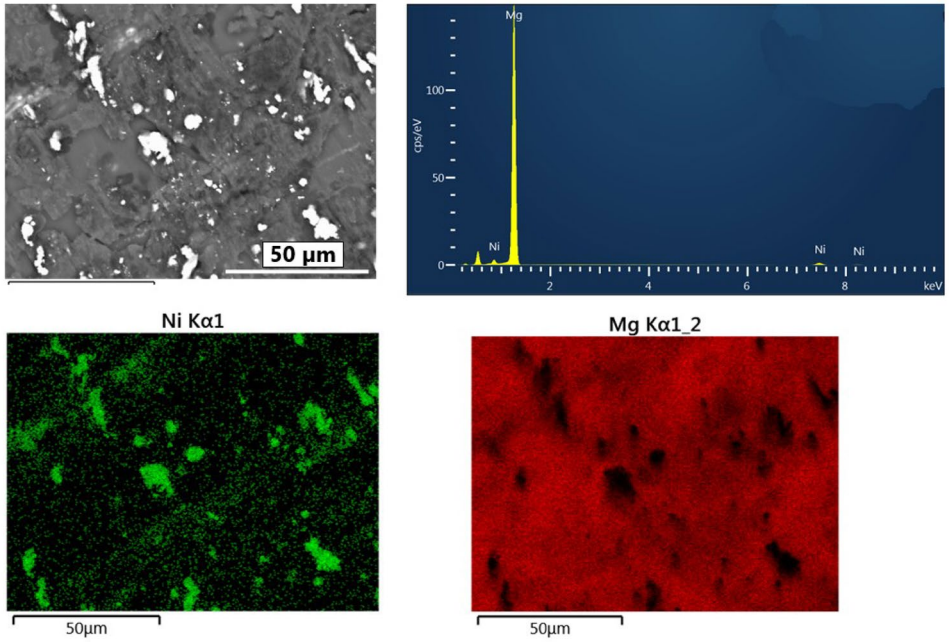

Fig. 7 EDS Mapping of Phases in an MgNi2 composite

[27, 59] and TiFe-based [60] hydrides, where high-Pressure DSC transition temperatures as a function of hydrogen pressure have been combined with van't Hoff analysis to obtain enthalpy and entropy values. To minimize the influence of kinetic effects and thermal gradients, thermodynamic parameters were derived from DSC measurements conducted at a slow heating rate of 2 $K \cdot min^{-1}$. The onset temperatures of the dehydrogenation and hydrogenation peaks were taken as approximations of the equilibrium temperatures. Although the non-isothermal nature of DSC causes a systematic deviation relative to fully isothermal PCT measurements, using a single, consistent onset-temperature criterion for all compositions and pressures provides internal consistency in the extracted ΔH and ΔS values. This approach, combined with slow heating rates, ensures that the derived values ΔH and ΔS provide a consistent comparative analysis among the extracted parameters.

For the MgNi16-N0 sample at 2 $K \cdot min^{-1}$, the derived thermodynamic parameters were obtained as: $\Delta H = 72 \pm 2$ $kJ \cdot mol^{-1}$ and $\Delta S = 132 \pm 3$ $J \cdot mol^{-1} \cdot K^{-1}$ for Mg_2NiH_4 dehydrogenation, and $\Delta H = 77 \pm 3$ $kJ \cdot mol^{-1}$ and $\Delta S = 137 \pm 5$ $J \cdot mol^{-1} \cdot K^{-1}$ for MgH_2 dehydrogenation. These values are in reasonable agreement with the available literature data for these hydride systems [61–65]. Hydrogenation thermodynamics were similarly analyzed using van't Hoff plots constructed from cooling ramp data at 2 $K \cdot min^{-1}$ (Fig. 10). The Mg hydrogenation exhibited $\Delta H = -69 \pm 4$ $kJ \cdot mol^{-1}$ and $\Delta S = 128 \pm 7$ $J \cdot mol^{-1} \cdot K^{-1}$, while Mg_2Ni hydrogenation showed $\Delta H = -62 \pm 3$ $kJ \cdot mol^{-1}$ and $\Delta S = 120 \pm 3$ $J \cdot mol^{-1} \cdot K^{-1}$.

Hysteresis analysis

Upon comparing the enthalpy and entropy values in hydrogenation with respect to those obtained for dehydrogenation, some differences in their magnitudes are observed. These discrepancies between the absorption and desorption processes indicate deviations from ideal thermodynamic reversibility, a phenomenon commonly referred to as hysteresis in hydrogen storage systems[66]. This thermodynamic parameter provides fundamental insights into the energy landscape of the hydrogen sorption process, revealing the stability of the hydride phase and the reversibility of the hydrogen storage reaction [67, 68]. The thermodynamic hysteresis represents the energy loss and total irreversibility of a full hydrogen storage cycle based on the enthalpy and entropy derived from van't Hoff plots.

Table 6 provides the enthalpy and entropy of dehydrogenation and hydrogenation for all samples following the van't Hoff methodology explained above. To allow for a direct and consistent comparison across all samples, the equilibrium pressures for dehydrogenation (P_{des}) and hydrogenation (P_{abs}) were calculated at a constant, representative temperature of 350 °C (623.15 K) using the van't Hoff equation (Eq. 4). This temperature was selected as representative of typical operating conditions for Mg-based hydrogen storage systems [67, 69–72]. The hysteresis was then expressed as a dimensionless hysteresis factor, defined as $\Delta Ln(P) = Ln(P_{abs} / P_{des})$, shown in Eq. (5). This factor provides a standardized measure of the deviation from ideal thermodynamic reversibility [73, 74].

$$\Delta LnP = Ln\left(P_{abs}\right) - Ln\left(P_{des}\right) = \frac{\Delta H_{abs} - \Delta H_{des}}{RT} + \frac{\Delta S_{abs} - \Delta S_{des}}{R} \quad (5)$$

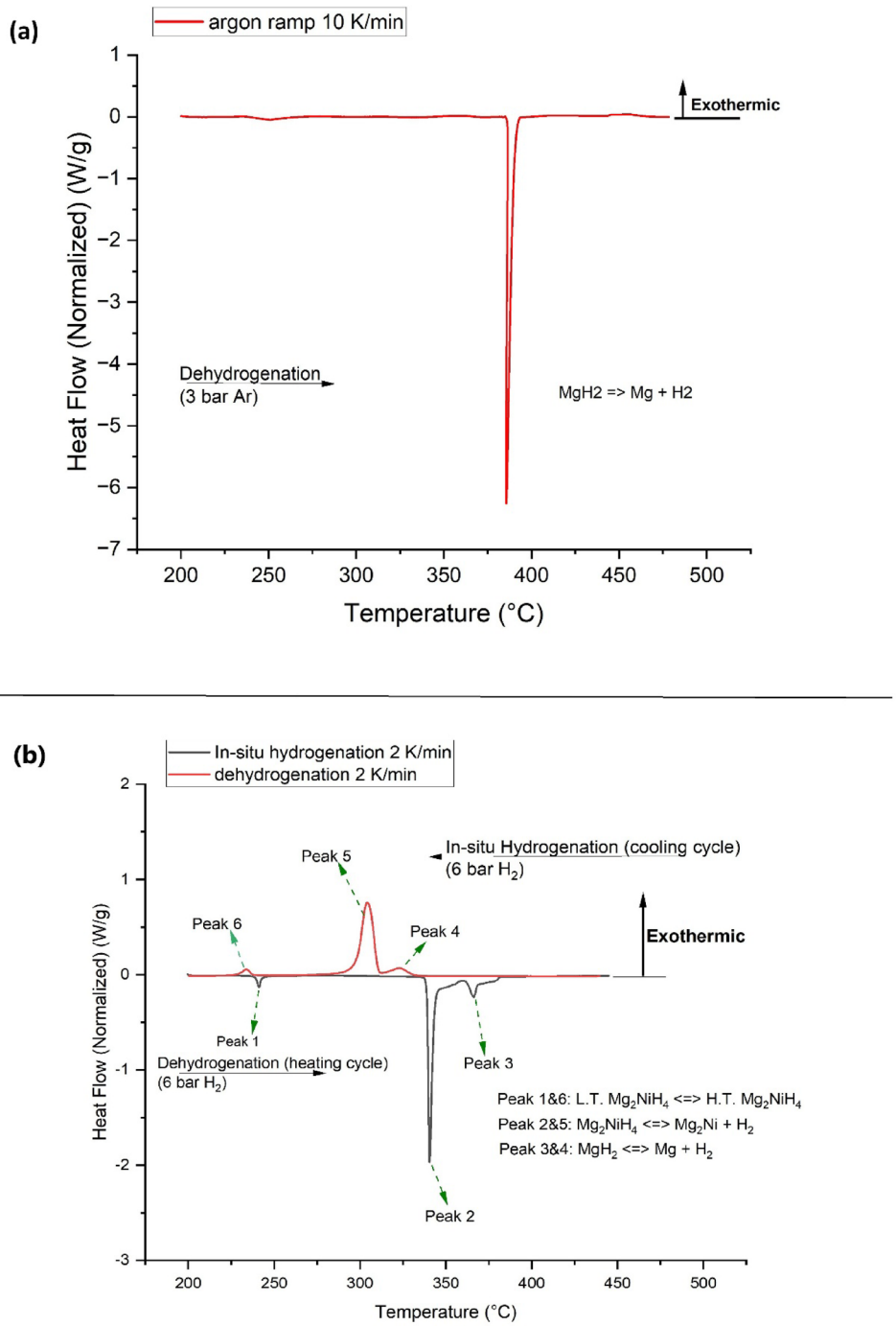

Fig. 8 DSC thermograms of an MgNi16-N0 sample. **a** Dehydrogenation of the sample under an argon atmosphere (3 bar) at a heating rate of 10 K.min^{-1}. **b** In-situ consecutive dehydrogenation and hydrogenation cycles under a hydrogen atmosphere (6 bar) at the heating/cooling rate of 2 K.min^{-1}

A comprehensive evaluation of the thermodynamic properties of all samples in de/hydrogenation and their hysteresis was conducted and summarized in Table 6.

It should be clarified that the effect of HPT in Table 6 is presented only for the MgNi16 series. For this composition, samples with 0, 1, and 5 HPT turns were analyzed to evaluate the influence of strain. Hysteresis values for MgNi16 across HPT conditions (N = 0, 1, 5) show no systematic trend (Mg_2NiH_4: $\Delta \ln P = 0.24–0.51$; MgH_2: $\Delta \ln P = 0.44–0.49$), consistent with the thermodynamic invariance observed for ΔH and ΔS. This is also valid considering the fact that DSC experiments on each sample were conducted over several cycles (under argon at different heating rates, and under hydrogen at different pressures) up to ~ 450 °C, which is far beyond the recrystallization temperature of the material (about 150–200 °C)[75]. At these high temperatures, the microstructural effects induced by HPT, such as grain refinement and increased defect density, are effectively annealed out [76]. As a result, the starting microstructure did not have a lasting influence on such properties. Therefore, only the

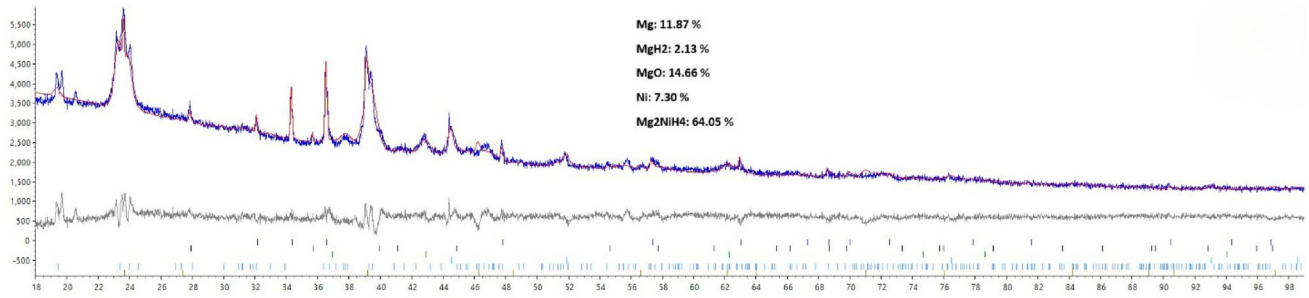

Fig. 9 Rietveld refinement of the MgNi16 sample after multiple dehydrogenation-hydrogenation cycles in the DSC. The final hydrogenation cycle was performed under a hydrogen atmosphere at 6 bar before cooling to room temperature for analysis

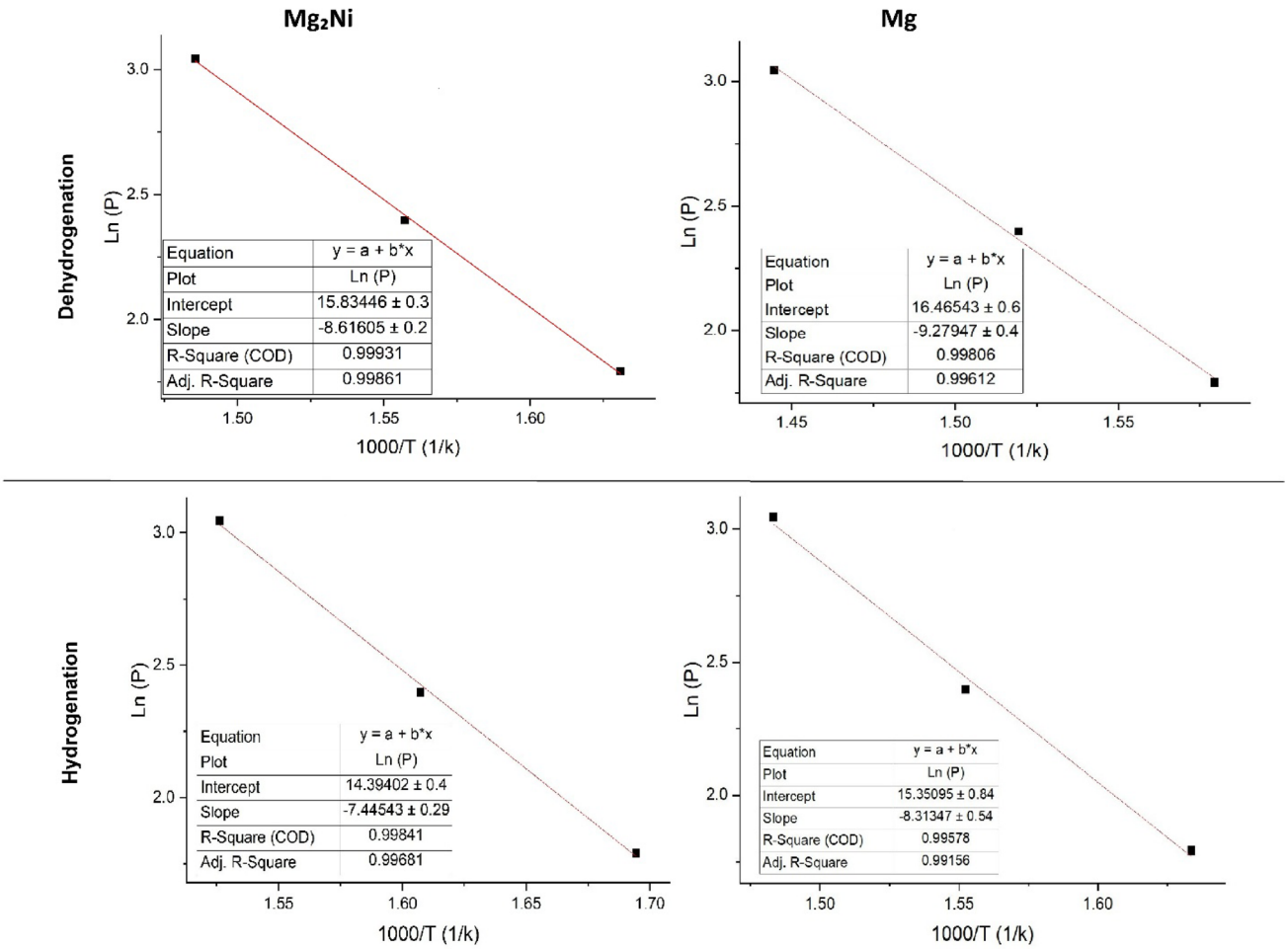

Fig. 10 Van't Hoff plots for the de/hydrogenation peaks of the MgNi16-N0 sample

five-turn HPT condition was included in the remaining compositions (MgNi2, MgNi4, and MgNi6), since preliminary results showed no obvious change beyond the error margins in ΔH or ΔS.

A direct comparison of the results in this table shows that Mg_2NiH_4 dehydrogenation is slightly less endothermic than that of MgH_2. This observation agrees with the well-known thermodynamic order of these hydrides [77] and also confirms that the DSC method used here can distinguish the stability of the two coexisting phases. The hysteresis values (ΔlnP) presented in Table 6 provide an overview of the reversibility of hydrogen cycling in the investigated samples. For the Mg_2NiH_4 phase, a wider scatter is observed (ΔLnP ≈ 0.24–0.95), whereas the MgH_2 phase exhibits more consistent hysteresis values across all compositions (ΔLnP ≈ 0.44–0.56).

Table 6 Thermodynamic parameters for the dehydrogenation and hydrogenation peaks of Mg-Ni–H composites derived from van't Hoff plots

Sample ID	HPT turns	Dehydrogenation		Hydrogenation		Hysteresis
		Enthalpy ($kJ \cdot mol^{-1}$)	Entropy ($J.mol^{-1} \cdot K^{-1}$)	Enthalpy ($kJ \cdot mol^{-1}$)	Entropy ($J.mol^{-1} \cdot K^{-1}$)	ΔLn (P)
Mg_2NiH_4						
MgNi2	5	73 ± 3	133 ± 2	− 59 ± 2	116 ± 2	0.51
MgNi4	5	73 ± 3	132 ± 5	− 61 ± 2	119 ± 2	0.63
MgNi6	5	72 ± 5	131 ± 5	− 61 ± 2	122 ± 4	0.95
MgNi16	0	72 ± 2	132 ± 3	− 62 ± 3	120 ± 3	0.43
MgNi16	1	70 ± 3	130 ± 2	− 63 ± 2	121 ± 2	0.24
MgNi16	5	71 ± 2	131 ± 4	− 62 ± 2	121 ± 1	0.51
MgH_2						
MgNi2	5	79 ± 3	139 ± 7	− 66 ± 3	123 ± 4	0.56
MgNi4	5	78 ± 3	137 ± 5	− 67 ± 4	124 ± 4	0.54
MgNi6	5	78 ± 5	137 ± 5	− 67 ± 3	125 ± 2	0.54
MgNi16	0	77 ± 3	137 ± 5	− 69 ± 4	128 ± 7	0.44
MgNi16	1	76 ± 3	135 ± 4	− 71 ± 4	131 ± 6	0.47
MgNi16	5	77 ± 3	136 ± 5	− 71 ± 4	131 ± 4	0.49

The error values for the enthalpy and entropy were obtained from the linear regression analysis of the van't Hoff plots

Discussion

Composition versus microstructure: relative contributions to hydrogen storage performance

The results presented above demonstrate that compositional tuning, specifically through nickel content, has a dominant influence on hydrogen storage performance compared to microstructural refinement via HPT processing. From a kinetic perspective, activation energy analysis (Table 4, Sect. "Activation energy analysis") reveals that increasing Ni content from 2 to 16 at% reduces E_a from 181 to 156 $kJ \cdot mol^{-1}$ for MgH_2 dehydrogenation, a reduction of approximately 14%. In contrast, HPT processing yields a reduction of approximately 21 $kJ \cdot mol^{-1}$ or 12% specifically in the MgNi16 samples after five turns of rotation.

The first hydrogenation curves (Fig. 2) further illustrate this hierarchy. MgNi2 and MgNi4 samples achieved less than 1 wt% H_2 uptake within 24 h regardless of HPT turns (N = 1 or N = 5), indicating that microstructural refinement alone cannot overcome insufficient catalytic activity. A threshold effect emerges at 6 at% Ni, where MgNi6-N5 reached 1.5 wt%, that is more than twofold improvement. The MgNi16 composition achieved 3.3 wt% (N = 5), demonstrating that adequate Ni content is a prerequisite for effective hydrogen activation. Within the MgNi16 series, HPT processing provided measurable but secondary benefits: MgNi16-N0 reached 2.8 wt% versus 3.3 wt% for MgNi16-N5, an 18% relative improvement related to grain refinement and crystalline defects.

From a thermodynamic perspective, this pattern becomes even clearer. Table 6 shows that enthalpy and entropy values remain largely constant across HPT conditions (comparing N = 0, N = 1, N = 5 for MgNi16) and show only minor variations across compositions. For example, MgH_2 dehydrogenation enthalpy ranges from 77 to 79 $kJ \cdot mol^{-1}$ across all samples, which is within experimental uncertainty. This insensitivity to both composition and microstructure reflects the fact that thermodynamic parameters are determined by the chemical nature of the hydride phases (MgH_2 vs. Mg_2NiH_4), whereas grain refinement and defect density mainly influence the reaction kinetics [19, 67].

The observed thermodynamic invariance with respect to HPT is attributed to thermal annealing during DSC cycling. Repeated heating to ~ 450 °C during in-situ measurements far exceeds magnesium's recrystallization temperature (~ 150–200 °C) [75], effectively erasing the nanostructure imposed by HPT. From a practical standpoint, these findings suggest that HPT or similar SPD processing may be valuable for initial material activation and first hydrogenation kinetics enhancement, whereas sustained cycling performance can be largely ensured by appropriate catalytic alloying. For laboratory-scale fundamental studies, HPT offers excellent control over microstructure and enables systematic investigation of deformation effects. In contrast, compositional effects -particularly the catalytic role of nickel- remain active throughout cycling because they reflect intrinsic chemical properties rather than metastable microstructural features [26, 67, 78, 79]. Therefore, sufficient Ni content for in-situ Mg_2Ni formation provides persistent catalytic benefits that survive thermal cycling, even in large-scale applications.

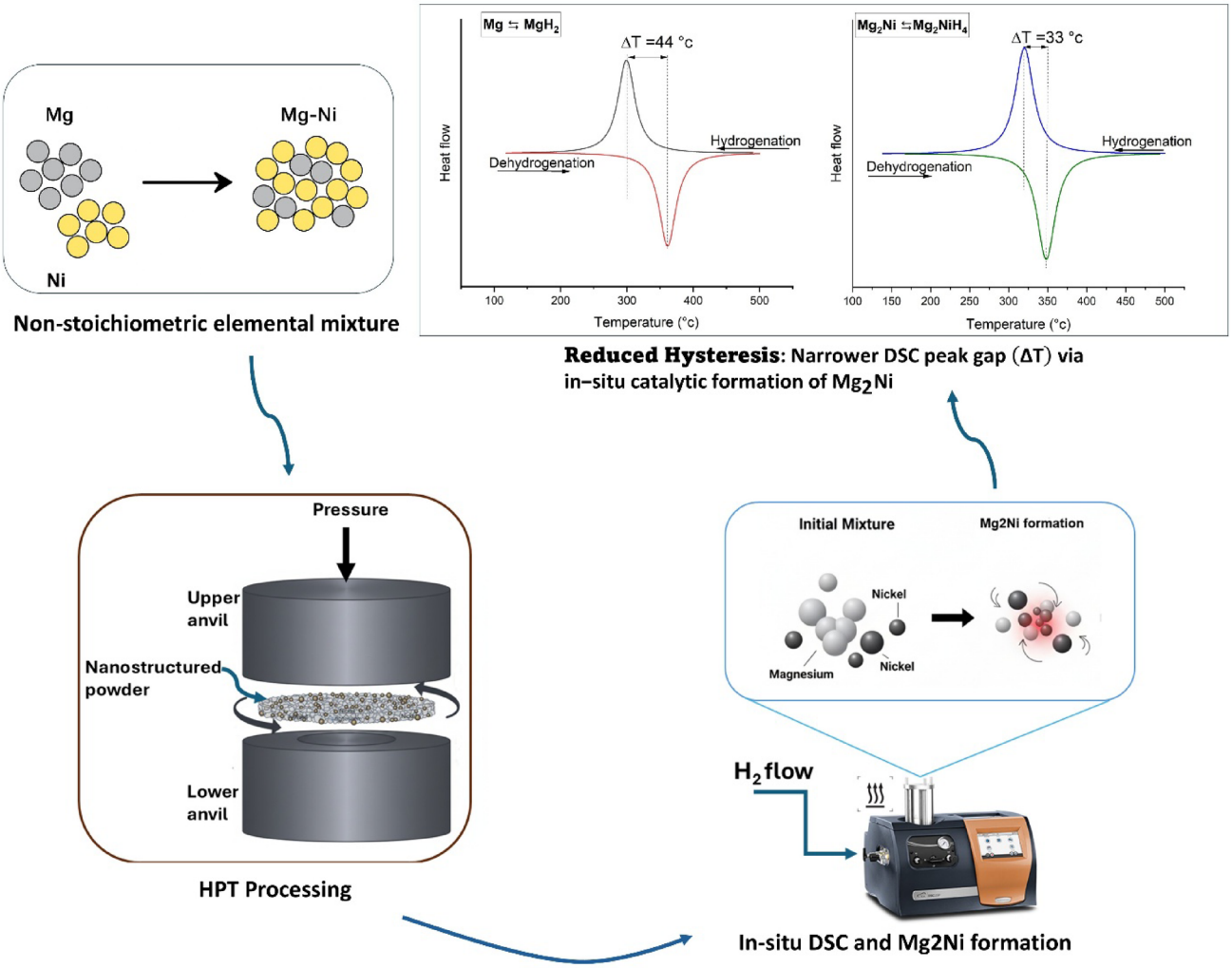

Fig. 11 Schematic illustration of the integrated processing and characterization approach in Mg-Ni composites. The workflow demonstrates the initial powder mixture to microstructural refinement (via HPT), in-situ Mg_2Ni phase synthesis during DSC thermal cycling, and the resulting reduction in hysteresis, evidenced by the narrowed separation (ΔT) of the de/hydrogenation peaks

In-situ Mg_2Ni formation

A central finding of this work is that Mg_2Ni forms in-situ during DSC thermal cycling from initially non-stoichiometric Mg-Ni powder mixtures, and this phase plays a critical role in subsequent hydrogen storage performance. XRD analysis after first hydrogenation in the Sievert apparatus (Fig. 5, Table 5) confirmed the presence of MgH_2, unreacted Mg, and Ni, but no Mg_2Ni intermetallic phase. However, post-DSC XRD (Fig. 9) revealed 64 wt% Mg_2NiH_4 in the MgNi16 sample after cycling under hydrogen, demonstrating that repeated exposure to elevated temperature and hydrogen pressure drives solid-state reaction between elemental Mg and Ni to form the Mg_2Ni intermetallic. This in-situ formation pathway differs from conventional synthesis routes (melting, ball milling) and offers practical advantages. Pre-alloyed Mg_2Ni requires either high-temperature metallurgical processing or extended mechanical milling, both energy- and time- intensive approaches [33, 80, 81]. In contrast, the present approach demonstrates that simple powder mixing, combined with HPT consolidation, achieves phase formation during hydrogen cycling via DSC. This pathway is particularly relevant for real-world applications where perfect stoichiometric control may not be guaranteed and when avoiding intermediate material processing complications.

This sequence of processing steps and their impact on phase evolution and hysteresis is summarized schematically in Fig. 11.

The catalytic mechanism of Mg_2Ni enhances the hydrogenation mechanism through three distinct pathways:

- First, the Mg_2Ni/Mg_2NiH_4 system exhibits lower thermodynamic stability than MgH_2/Mg, as evidenced by the

lower decomposition temperature (~350°C vs.~390°C in DSC thermograms, Fig. 8-b) and reduced enthalpy values (72 vs. 77 kJ·mol^{-1} for dehydrogenation, Table 6). This thermodynamic advantage enables hydrogen release and uptake at more favorable conditions.

- Second, Mg_2Ni provides active surface sites for H_2 dissociation and recombination, lowering the kinetic barrier reflected in reduced activation energies [52, 53, 82].
- Third, the presence of Mg_2Ni creates interfacial regions with Mg/MgH_2 that may serve as preferential nucleation sites for hydride formation and decomposition[68, 83, 84].

The compositional range investigated (2–16 at% Ni) reveals that Mg_2Ni formation and its catalytic benefits require sufficient Ni content. At 2–4 at% Ni, sufficient elemental Ni is unavailable for hydrogenation, resulting in limited catalytic enhancement. At 6 at% Ni, it could measurably improve kinetics (see Fig. 2), and at 16 at% Ni, Mg_2Ni formation is maximized (as evidenced by 64 wt% Mg_2NiH_4 -as revealed by the Rietveld analysis- Fig. 9), yielding the lowest activation energies and fastest hydrogenation rates (see Fig. 2 & Fig. 4). This compositional window (6–16 at% Ni) defines a practical design space where non-stoichiometric Mg-Ni composites can achieve effective hydrogen storage performance through in-situ phase evolution. Importantly, even at 16 at% Ni, some elemental Mg remains unreacted (as Fig. 9 shows residual Mg after cycling). This multiphase coexistence—Mg_2Ni/Mg_2NiH_4 alongside MgH_2/Mg—results in the dual-peak DSC behavior observed (Peaks 2 and 3 in Fig. 8b). While this complicates thermodynamic analysis compared to pure single-phase systems, it may actually be advantageous for applications requiring staged hydrogen release across a temperature range.

The observed 14.7 wt% MgO in MgNi16-N0 after DSC cycling (Fig. 9) formed during sample handling, represents Mg permanently removed from the Mg-Ni reaction. Since Mg oxidizes preferentially over Ni, this effectively enriches the Ni concentration in the remaining reactive material [68], while the Mg_2NiH_4 phase reaches 64 wt%. Literature on Mg_2Ni formation shows composition- and kinetics-limited saturation behavior. Ball-milling studies demonstrate that even after extended processing time and then annealing, complete Mg_2Ni conversion is rarely achieved, with residual phases persisting due to diffusion-limited reactions and product-layer formation that blocks further conversion [53, 85]. Cycling-assisted formation studies show that Mg_2Ni fractions increase over the first few cycles and then plateau, with further cycling primarily refining microstructure rather than changing the overall phase balance [86]. Even hydrogen-assisted pathways (such as using MgH_2 as starting materials), which accelerate interdiffusion compared to solid-state annealing, remain diffusion-limited and composition-dependent [12, 25]. These precedents indicate that phase fractions tend to reach a composition-dependent saturation rather than increasing indefinitely. In this work, the residual 7.3 wt% Ni is therefore likely kinetically trapped, for example as Ni-rich particles surrounded by Mg_2Ni product layers or adjacent to MgO interfaces. Further conversion would require more aggressive processing (high-temperature annealing, re-milling), which is incompatible with DSC cycling. Based on these observations and the presence of kinetically trapped residual Ni, additional DSC cycling is unlikely to substantially increase Mg_2Ni fraction beyond~64 wt%. Importantly, this level already provides sufficient catalytic enhancement (activation energy reduction from 181 to 156 kJ·mol^{-1} and markedly faster absorption), so the observed saturation is practically effective despite incomplete conversion.

Practical implications for material design

The findings of this study provide several insights for designing Mg-based hydrogen storage materials:

1. Compositional optimization over microstructural refinement: For systems where thermal cycling is anticipated, efforts should prioritize compositional design (catalytic additives) over metastable nanostructuring, as compositional effects persist while nanostructure anneals out. Nickel content in the 6–16 at% range provides substantial benefits, whereas below 6 at%, catalytic effects are insufficient for practical kinetics. SPD techniques like HPT are valuable for laboratory studies and for accelerating initial activation but are not essential for long-term performance. For scaled production, if rapid initial activation is critical, brief high-temperature treatment under hydrogen may substitute for intensive mechanical nanostructuring. This highlights that while SPD techniques like HPT are excellent for creating high-density interfaces for initial activation, the long-term performance is dominated by the thermodynamically stable Mg_2Ni catalyst.
2. Non-stoichiometric processing flexibility: Perfect stoichiometric control (e.g., exactly Mg_2Ni) is not required. Elemental Mg-Ni powder mixtures with appropriate Ni content will form active Mg_2Ni during thermal cycling under hydrogen. This simplifies processing and allows compositional tuning without requiring pre-alloying steps. The multiphase nature (coexisting Mg/MgH_2 and Mg_2Ni/Mg_2NiH_4) may even be advantageous for applications requiring staged hydrogen release.
3. Operating temperature selection: The in-situ formation of Mg_2Ni requires elevated temperature exposure during

initial cycling (demonstrated here at ~ 550 °C under hydrogen). For practical applications, the system must allow for a one-time activation step to establish the new phase. Once Mg_2Ni is formed, subsequent cycling can occur at lower temperatures (~ 350–400 °C) while retaining catalytic benefits.

4. Balancing capacity and kinetics: Higher Ni content improves kinetics but reduces gravimetric capacity (Mg_2NiH_4 stores 3.6 wt% H_2 vs. 7.6 wt% for MgH_2)[25, 87]. The optimal composition depends on application requirements; systems prioritizing fast kinetics and moderate capacity may favor 8–16 at% Ni, while capacity-critical applications could use 4–6 at% Ni with longer activation times.

Scientific context and research significance

The thermodynamic parameters obtained here (ΔH = 70–73 $kJ \cdot mol^{-1}$ for Mg_2NiH_4; 77–79 $kJ \cdot mol^{-1}$ for MgH_2) show a moderate positive deviation from typical equilibrium values obtained from isothermal PCT measurements [61–65, 88]. Similar deviations have been observed in earlier DSC-based studies of Mg hydrides [59] as well as other hydride systems [27, 89, 90]. This systematic deviation is well-documented for non-equilibrium thermal analysis methods, where finite heating rates produce apparent enthalpies 5–20% higher than true equilibrium values due to thermal lag, incomplete phase equilibration, and kinetic contributions [56, 87, 91]. While Révész et al. [11] examined HPT-processed stoichiometric Mg_2Ni using similar DSC methodology, the present work bridges a critical gap by investigating a non-stoichiometric compositional range (2–16 at% Ni), providing a comprehensive framework for understanding the practical processing of Mg-Ni composites for hydrogen storage applications.

Finally, it should be acknowledged that the slow kinetics observed in the first Sievert hydrogenation largely reflect the typical activation process of magnesium-based hydrides, often requiring extended times and, in our case, not reaching full capacity even after 24 h. However, the subsequent DSC measurements revealed a faster hydrogenation process with the DSC peaks indicating nearly complete hydrogenation signals within relatively shorter timeframes. This difference between Sievert and DSC kinetics is not solely a first-cycle effect, but also reflects the catalytic role of in-situ formation of Mg_2Ni, which is absent in the pristine Mg–Ni powder mixture. Once Mg_2Ni forms in-situ during the dehydrogenation cycles in DSC (Eq. 3), it acts as a catalyst in the subsequent DSC hydrogenations, accelerating hydrogen uptake.

As shown in Fig. 8, the first dehydrogenation peak during DSC cycling originated from Mg_2NiH_4 at lower temperatures prior to MgH_2, indicating a lower activation barrier pathway. While the in-situ formation of Mg_2Ni as a catalytic phase has been well recognized by ball milling [33], our study demonstrates that such phase evolution can be directly induced and tracked using in-situ DSC. This methodological approach, applied to HPT-processed composites, provides a facile route to quantify the thermodynamic parameters while capturing the catalytic role of in-situ formed Mg_2Ni. Thus, catalytic phase formation during in-situ DSC cycling from non-stoichiometric powders offers a viable pathway for improving hydrogen storage performance without the need for perfectly pre-alloyed compounds.

Conclusion

This study investigated the combined effects of nickel content (2–16 at%) and High Pressure Torsion (HPT) on the hydrogen storage performance of Mg-Ni powder mixtures. The results demonstrate that compositional tuning dominates over microstructural refinement in hydrogen sorption performance.

Kinetics: Activation energy analysis via the Kissinger method revealed that increasing Ni content from 2 to 16 at% reduced the kinetic barrier for MgH_2 dehydrogenation from 181 to 156 $kJ \cdot mol^{-}1$, a 14% reduction. HPT processing provided additional improvements (~ 12%) in initial activation, with the effect being most pronounced when sufficient Ni was present. First hydrogenation kinetics using the Sievert apparatus confirmed that compositions with less than 6 at% Ni achieved minimal uptake (< 1 wt% in 24 h) regardless of HPT turns, while the sample with 16 at% Ni and after five turns of HPT rotations (MgNi16-N5) reached 3.3 wt%, demonstrating that adequate Ni content is a prerequisite for effective hydrogen activation.

Thermodynamic: In-situ differential scanning calorimetry (DSC) cycling was implemented to characterize the thermodynamic properties via van't Hoff analysis. The results demonstrated that enthalpy and entropy values remained invariant across all investigated Ni concentrations and HPT processing conditions. This stability indicates that the fundamental thermodynamic equilibrium is not significantly altered by microstructural refinement or the presence of the catalytic phase. The lack of microstructural influence is attributed to thermal annealing during DSC cycling (up to ~ 450 °C), which exceeds the recrystallization temperature of magnesium and leads to the recovery of the HPT-induced features. Consequently, while HPT and Ni-addition effectively optimize the kinetic pathways, they do not shift the intrinsic thermodynamic stability of the hydride phases Mg_2NiH_4 and MgH_2.

Phase evolution: A key finding is that Mg_2Ni forms in-situ during DSC cycling from non-stoichiometric Mg-Ni

powder mixtures. XRD analysis confirmed that the Mg_2Ni intermetallic, absent after the initial Sievert hydrogenation, formed during DSC cycling under elevated temperature and hydrogen pressure, with Rietveld refinement indicating 64 wt% Mg_2NiH_4 in the sample with 16 at% Ni (MgNi16). This in-situ formation pathway provides practical advantages over conventional synthesis routes, e.g., ball milling, as it eliminates the need for complex pre-alloying and provides a flexible approach to material synthesis. The catalytic role of Mg_2Ni, evidenced by lower decomposition temperatures (~350 °C vs.~390 °C for MgH_2) and reduced activation energies, remains active throughout cycling. Exploiting non-stoichiometric Mg-Ni composites and achieving effective hydrogen storage performance through in-situ phase evolution provides a more flexible and practical pathway for material development compared to traditional techniques requiring perfect stoichiometry.

Practical implications: These findings provide several key principles for the strategic design of Mg-based storage systems: (1) The results suggest that compositional optimization (6–16 at% Ni) should be considered a priority over intensive mechanical processing for achieving sustained performance. (2) Perfect stoichiometric control is unnecessary, as active phases form in-situ from elemental mixtures; (3) An initial high-temperature activation (~550 °C) via DSC facilitates the formation of Mg_2Ni, after which the system can operate efficiently at significantly lower temperatures (350–400 °C); (4) Ni content can be balanced based on application requirements: higher Ni improves kinetics but reduces capacity. (5) The dominance of composition over microstructure suggests that cost-effective processing strategies can be realized by shifting the focus toward targeted chemical additions and in-situ phase engineering.

Acknowledgements This project was funded in part by the Marie-Sklodowska Curie (MSCA) grant No. 847635.

Data Availability The data that support the findings of this study are available from the corresponding author upon reasonable request.

References

1. Xu, Y., Zhou, Y., Li, Y., Hao, Y., Wu, P., Ding, Z.: Magnesium-based hydrogen storage alloys: advances, strategies, and future outlook for clean energy applications. Molecules **29**(11), 2525 (2024). https://doi.org/10.3390/molecules29112525
2. Ren, L., Li, Y., Zhang, N., Li, Z., Lin, X., Zhu, W., et al.: Nanostructuring of Mg-based hydrogen storage materials: recent advances for promoting key applications. Nano-Micro Lett. (2023). https://doi.org/10.1007/s40820-023-01041-5
3. Li, X., Yuan, Z., Liu, C., Sui, Y., Zhai, T., Hou, Z., et al.: Research progress in improved hydrogen storage properties of Mg-based alloys with metal-based materials and light metals. Int. J. Hydrogen Energy **50**, 1401–1417 (2024). https://doi.org/10.1016/j.ijhydene.2023.09.265
4. Xu, Y., Zhou, Y., Li, Y., Hao, Y., Wu, P., Ding, Z.: Recent advances in the preparation methods of Magnesium-based hydrogen storage materials. Molecules (2024). https://doi.org/10.3390/molecules29112451
5. Song, Y., Guo, Z.X., Yang, R.: Influence of selected alloying elements on the stability of magnesium dihydride for hydrogen storage applications: a first-principles investigation. Phys. Rev. B **69**(9), 094205 (2004). https://doi.org/10.1103/PhysRevB.69.094205
6. Huot, J., Ravnsbæk, D.B., Zhang, J., Cuevas, F., Latroche, M., Jensen, T.R.: Mechanochemical synthesis of hydrogen storage materials. Prog. Mater. Sci. **58**(1), 30–75 (2013). https://doi.org/10.1016/j.pmatsci.2012.07.001
7. Zhou, C., Zhang, J., Bowman, R.C., Fang, Z.Z.: Roles of Ti-based catalysts on magnesium hydride and its hydrogen storage properties. Inorganics. **9**(5), 36 (2021). https://doi.org/10.3390/inorganics9050036
8. Sun, Z., Lu, X., Nyahuma, F.M., Yan, N., Xiao, J., Su, S., et al.: Enhancing hydrogen storage properties of MgH2 by transition metals and carbon materials: a brief review. Front. Chem. (2020). https://doi.org/10.3389/fchem.2020.00552
9. Omranpour Shahreza, B., Ivanisenko, J., Sergejev, F., Omranpour, H., Huot, J.: A novel approach in mechanical nanostructuring synthesis of metal hydride: hydrogen sorption enhancement by high pressure torsion extrusion. Int. J. Hydrogen Energy **51**, 133–142 (2024). https://doi.org/10.1016/j.ijhydene.2023.10.343
10. Rozenberg, S., Saporiti, F., Lang, J., Audebert, F., Botta, P., Stoica, M., et al.: Effect of alloying elements in melt spun Mg-alloys for hydrogen storage. Mater. Res. (2016). https://doi.org/10.1590/1980-5373-MR-2016-0048
11. Révész, Á., Gajdics, M., Schafler, E., Calizzi, M., Pasquini, L.: Dehydrogenation-hydrogenation characteristics of nanocrystalline Mg_2Ni powders compacted by high-pressure torsion. J. Alloy. Compd. **702**, 84–91 (2017). https://doi.org/10.1016/j.jallcom.2017.01.261
12. Zhao, B., Fang, F., Sun, D., Zhang, Q., Wei, S., Cao, F., et al.: Formation of Mg_2Ni with enhanced kinetics: using MgH_2 instead of Mg as a starting material. J. Solid State Chem. **192**, 210–214 (2012). https://doi.org/10.1016/j.jssc.2012.04.011
13. Huot, J.: Nanocrystalline metal hydrides obtained by severe plastic deformations. Metals **2**, 22–40 (2012)
14. Leiva, D.R., Jorge, J.A.M., Ishikawa, T.T., Botta, W.J.: Hydrogen storage in Mg and Mg-based alloys and composites processed by severe plastic deformation. Mater. Trans. **60**(8), 1561–1570 (2019). https://doi.org/10.2320/matertrans.mf201927
15. Leiva, D.R., Jorge, A.M., Ishikawa, T.T., Huot, J., Fruchart, D., Miraglia, S., et al.: Nanoscale grain refinement and H-sorption properties of MgH2 processed by high-pressure torsion and other mechanical routes. Adv. Eng. Mater. **12**(8), 786–792 (2010). https://doi.org/10.1002/adem.201000030

16. Edalati, K.: Contribution of severe plastic deformation via high-pressure torsion to the hydrogen cycle: from hydrogen production and storage to hydrogen embrittlement. Hydrogen **7**(1), 23 (2026). https://doi.org/10.3390/hydrogen7010023
17. Rabkin, E., Skripnyuk, V., Estrin, Y.: Ultrafine-grained Magnesium alloys for hydrogen storage obtained by severe plastic deformation. Front. Mater. (2019). https://doi.org/10.3389/fmats.2019.00240
18. Hongo, T., Edalati, K., Arita, M., Matsuda, J., Akiba, E., Horita, Z.: Significance of grain boundaries and stacking faults on hydrogen storage properties of Mg2Ni intermetallics processed by high-pressure torsion. Acta Mater. **92**, 46–54 (2015). https://doi.org/10.1016/j.actamat.2015.03.036
19. Révész, Á., Gajdics, M.: The effect of severe plastic deformation on the hydrogen storage properties of metal hydrides. Mater. Trans. **64**(7), 1387–1400 (2023). https://doi.org/10.2320/matertrans.mt-mf2022019
20. Omranpour, H., Shahreza, B.O., Kheradmandkeysomi, M., Buahom, P., Monfared, A.R., Park, C.B.: Thermally insulated sub-100 µm aerogel fibers obtained by including chemically modified and aligned thermoplastic polyurethane nanofibrils and a prepolymerized silica precursor. ACS Appl. Nano Mater. (2025). https://doi.org/10.1021/acsanm.5c03856
21. Edalati, K., Akiba, E., Horita, Z.: High-pressure torsion for new hydrogen storage materials. Sci. Technol. Adv. Mater. **19**, 185–193 (2018). https://doi.org/10.1080/14686996.2018.1435131
22. Xu, Y., Zhou, Y., Li, Y., Hao, Y., Wu, P., Ding, Z.: Recent advances in the preparation methods of magnesium-based hydrogen storage materials. Molecules **29**(11), 2451 (2024). https://doi.org/10.3390/molecules29112451
23. Nobuki, T., Okuzumi, Y., Hatate, M., Crivello, J.-C., Cuevas, F., Joubert, J.-M.: Mechanosynthesis and reversible hydrogen storage of Mg_2Ni and Mg_2Cu alloys. Mater. Trans. **60**(3), 441–449 (2019). https://doi.org/10.2320/matertrans.m2018293
24. Yartys, V.A., Lototskyy, M.V., Akiba, E., Albert, R., Antonov, V.E., Ares, J.R., et al.: Magnesium based materials for hydrogen based energy storage: past, present and future. Int. J. Hydrogen Energy **44**(15), 7809–7859 (2019). https://doi.org/10.1016/j.ijhydene.2018.12.212
25. Lai, D.V., Nguyen, S.H., Nguyen, A.H., Nguyen, T.V., Dinh, L.C., Doan, P.D., et al.: Tailoring hydrogen storage performance of Mg-Mg2Ni alloys: synergistic effects of composition and phase formation with first-principles insights. RSC Adv. **15**(38), 31240–31254 (2025). https://doi.org/10.1039/D5RA04356E
26. Edalati, K., Akiba, E., Botta, W.J., Estrin, Y., Floriano, R., Fruchart, D., et al.: Impact of severe plastic deformation on kinetics and thermodynamics of hydrogen storage in magnesium and its alloys. J. Mater. Sci. Technol. **146**, 221–239 (2023). https://doi.org/10.1016/j.jmst.2022.10.068
27. Rongeat, C., Llamas-Jansa, I., Doppiu, S., Deledda, S., Borgschulte, A., Schultz, L., et al.: Determination of the heat of hydride formation/decomposition by high-pressure differential scanning calorimetry (HP-DSC). J. Phys. Chem. B **111**(46), 13301–13306 (2007). https://doi.org/10.1021/jp075954r
28. Skryabina, N., Medvedeva, N., Gabov, A., Fruchart, D., Nachev, S., de Rango, P.: Impact of severe plastic deformation on the stability of MgH2. J. Alloy. Compd. **645**, S14–S17 (2015). https://doi.org/10.1016/j.jallcom.2015.03.128
29. Révész, Á., Gajdics, M.: High-pressure torsion of non-equilibrium hydrogen storage materials: a review. Energies **14**(4), 819 (2021)
30. Kitabayashi, K., Edalati, K., Li, H.-W., Akiba, E., Horita, Z.: Phase Transformations in MgH2–TiH2 hydrogen storage system by high-pressure torsion process. Adv. Eng. Mater. **22**(1), 1900027 (2020). https://doi.org/10.1002/adem.201900027
31. Bönisch, M., Zehetbauer, M.J., Krystian, M., Setman, D., Krexner, G.: Stabilization of lattice defects in HPT-deformed palladium hydride. Mater. Sci. Forum **667–669**, 427–432 (2011). https://doi.org/10.4028/www.scientific.net/MSF.667-669.427
32. Cengeri, P., Kimoto, Y., Janoska, M., Abbasi, Z., Morisada, Y., Fujii, H., et al.: Long term hydrogen storage properties of ZK60 Mg-alloy as processed by different methods of SPD. J. Mater. Sci. **59**(14), 5906–5922 (2024). https://doi.org/10.1007/s10853-024-09529-0
33. Liu, X., Zhou, L., Li, W., Wu, S., Huang, Q., Wang, Y., et al.: Preparation of Mg2Ni hydrogen storage alloy materials by high energy ball milling. Adv. Mater. Sci. Eng. **2022**(1), 2661424 (2022). https://doi.org/10.1155/2022/2661424
34. Wang, X., Spratt, H.: Incorporating the direct derivation method and molecular scattering power method into the Rietveld quantitative phase analysis routine in *TOPAS*. J. Appl. Crystallogr. **58**(4), 1159–1173 (2025). https://doi.org/10.1107/s1600576725004054
35. Vrátná, J., Janeček, M., Stráský, J., Kim, H.S., Yoon, E.-Y.: Investigation of microhardness and microstructure of az31 alloy after high pressure torsion. In: Sillekens, W.H., Agnew, S.R., Neelameggham, N.R., Mathaudhu, S.N. (eds.) Magnesium Technology 2011, pp. 589–594. Springer International Publishing, Cham (2016)
36. Hassan, S.F., Gupta, M.: J. Mater. Sci. **37**(12), 2467–2474 (2002). https://doi.org/10.1023/a:1015475103720
37. Fibela-Esparza, M., Salinas-Rodriguez, A., Méndez-Nonell, J., Herrera-Ramirez, J.M., Todaka, Y., Cabañas-Moreno, J.G.: Mg-Ni-Nb2O5 composite produced by high-pressure torsion. Metals **12**(10), 1684 (2022). https://doi.org/10.3390/met12101684
38. Hassan, S.F., Nasirudeen, O.O., Al-Aqeeli, N., Saheb, N., Patel, F., Baig, M.M.A.: Magnesium–nickel composite: preparation, microstructure and mechanical properties. J. Alloys Compd. **646**, 333–338 (2015). https://doi.org/10.1016/j.jallcom.2015.06.099
39. Chiu, C., Lee, H.-W., Yeh, M.-T., Yen, H.-W., Lin, H.-C.: Effects of short-term mechanical milling and catalyst on the hydrogen storage performance of ZK60 alloy modified by mischmetal and severe plastic deformation. Int. J. Hydrogen Energy **160**, 150626 (2025). https://doi.org/10.1016/j.ijhydene.2025.150626
40. Song, M.-Y., Kwak, Y.-J.: Determination of the activation energy for hydride decomposition using a Sieverts-type apparatus and the Kissinger equation. Metals **12**(2), 265 (2022). https://doi.org/10.3390/met12020265
41. Qi, Y., Zhou, D., Sun, W., Li, J., Cao, Z., Xu, L., et al.: Improving hydrogen storage characteristics of Mg–Ni-based alloys by adding Y and melt spinning. J. Phys. Chem. Solids **208**, 113027 (2026). https://doi.org/10.1016/j.jpcs.2025.113027
42. Cortínez, J.S., Gómez, A., Zuleta, A.A., Tamayo, J.A., Correa, E., Bolívar, F.J., et al.: Improved hydrogen storage in magnesium thin flakes via nickel and titanium/titanium carbide additives. Int. J. Hydrogen Energy **153**, 150264 (2025). https://doi.org/10.1016/j.ijhydene.2025.150264
43. Perejón, A., Sánchez-Jiménez, P.E., Criado, J.M., Pérez-Maqueda, L.A.: Magnesium hydride for energy storage applications: the kinetics of dehydrogenation under different working conditions. J. Alloys Compd. **681**, 571–579 (2016). https://doi.org/10.1016/j.jallcom.2016.04.191
44. Xuanhui, Q., Ping, L., Zhang, L., Ahmad, M., Iqbal, M.Z., et al.: Enhanced hydrogen storage performance for MgH 2–NaAlH 4 system—the effects of stoichiometry and Nb_2O_5 nanoparticles on cycling behaviour. RSC Adv. **2**(11), 4891–4903 (2012). https://doi.org/10.1039/C2RA20518A
45. Ismail, M., Yahya, M.S., Sazelee, N.A., Ali, N.A., Yap, F.A.H., Mustafa, N.S.: The effect of K2SiF6 on the MgH2 hydrogen storage properties. J. Magnesium Alloys **8**(3), 832–840 (2020). https://doi.org/10.1016/j.jma.2020.04.002

46. Tome, K.C., Xi, S., Fu, Y., Lu, C., Lu, N., Guan, M., et al.: Remarkable catalytic effect of Ni and ZrO2 nanoparticles on the hydrogen sorption properties of MgH2. Int. J. Hydrogen Energy **47**(7), 4716–4724 (2022). https://doi.org/10.1016/j.ijhydene.2021.11.102
47. Ocampo, R.A., Arias-Velandia, J., Lenis, J.A., Gil, A.A.Z., Bello, S., Correa, E., et al.: Microwave-assisted synthesis of MgH2 nanoparticles for hydrogen storage applications. J. Nanopart. Res. (2025). https://doi.org/10.1007/s11051-025-06217-1
48. Li, W., Yang, X., Hou, Q., Lu, X., Kong, J., Su, J.: Modification of MgH(2) hydrogen storage performance by nickel-based composite catalyst Ni/NiO. Heliyon **10**(9), e30688 (2024). https://doi.org/10.1016/j.heliyon.2024.e30688
49. Jensen, T., Andreasen, A., Vegge, T., Andreasen, J., Stahl, K., Pedersen, A., et al.: Dehydrogenation kinetics of pure and nickel-doped magnesium hydride investigated by in situ time-resolved powder X-ray diffraction. Int. J. Hydrogen Energy **31**(14), 2052–2062 (2006). https://doi.org/10.1016/j.ijhydene.2006.02.004
50. Baraban, A.P., Dmitriev, V.A., Gabis, I.E., Voyt, A.P., Klyamkin, S.N., Shikin, I.V.: Direct synthesis of Mg2NiH4 from MgH2 and Ni. Phys. Complex Syst. **4**(3), 94–102 (2023). https://doi.org/10.33910/2687-153x-2023-4-3-94-102
51. Wang, P., Wang, Z., Tian, Z., Xia, C., Yang, T., Liang, C., et al.: Enhanced hydrogen absorption and desorption properties of MgH2 with NiS2: The catalytic effect of in-situ formed MgS and Mg2NiH4 phases. Renew. Energy **160**, 409–417 (2020). https://doi.org/10.1016/j.renene.2020.07.014
52. Ma, Z., Zhao, Y., Wu, Z., Tang, Q., Ni, J., Zhu, Y., et al.: Air-stable magnesium nickel hydride with autocatalytic and self-protective effect for reversible hydrogen storage. Nano Res. **15**(3), 2130–2137 (2022). https://doi.org/10.1007/s12274-021-3846-5
53. Sharma, B., Tiwari, S., Sharma, P.: Synthesis of Mg2Ni using stoichiometric and superstoichiometric compositions for hydrogen storage applications. Energy Storage. **3**(6), e262 (2021). https://doi.org/10.1002/est2.262
54. Zolliker, P., Yvon, K., Jorgensen, J.D., Rotella, F.J.: Structural studies of the hydrogen storage material magnesium nickel hydride (Mg2NiH4). 2. Monoclinic low-temperature structure. Inorg. Chem. **25**(20), 3590–3593 (1986). https://doi.org/10.1021/ic00240a012
55. Yvon, K., Schefer, J., Stucki, F.: Structural studies of the hydrogen storage material Mg2NiH4. 1. Cubic high-temperature structure. Inorg. Chem. **20**(9), 2776–2778 (1981). https://doi.org/10.1021/ic50223a006
56. Li, Q., Lu, Y., Luo, Q., Yang, X., Yang, Y., Tan, J., et al.: Thermodynamics and kinetics of hydriding and dehydriding reactions in Mg-based hydrogen storage materials. J. Magnesium Alloys. **9**(6), 1922–1941 (2021). https://doi.org/10.1016/j.jma.2021.10.002
57. Kwak, R.-H., Kim, D.-H., Park, H.-K.: Optimization of metal hydride material and evaluation of metal hydride tank for hydrogen-powered micromobility. Int. J. Hydrogen Energy **116**, 128–138 (2025). https://doi.org/10.1016/j.ijhydene.2025.03.079
58. Paul, A.R., Mehla, S., Bhargava, S.: Intermetallic compounds for hydrogen storage: current status and future perspectives. Small **21**(14), 2408889 (2025). https://doi.org/10.1002/smll.202408889
59. Urretavizcaya, G., Fuster, V., Castro, F.J.: High pressure DSC study of hydrogen sorption in MgH2/graphite mixtures: Effects of sintering and oxidation. Int. J. Hydrogen Energy **36**(9), 5411–5417 (2011). https://doi.org/10.1016/j.ijhydene.2011.02.025
60. Pericoli, E., Ferretti, V., Verna, D., Pasquini, L.: Tuning TiFe1–xNix hydride thermodynamics through compositional tailoring. ACS Appl. Energy Mater. **8**(4), 2135–2144 (2025). https://doi.org/10.1021/acsaem.4c02625
61. Yu, H., Bennici, S., Auroux, A.: Hydrogen storage and release: Kinetic and thermodynamic studies of MgH2 activated by transition metal nanoparticles. Int. J. Hydrogen Energy **39**(22), 11633–11641 (2014). https://doi.org/10.1016/j.ijhydene.2014.05.069
62. Yang, H., Ding, Z., Li, Y.-T., Li, S.-Y., Wu, P.-K., Hou, Q.-H., et al.: Recent advances in kinetic and thermodynamic regulation of magnesium hydride for hydrogen storage. Rare Met. **42**(9), 2906–2927 (2023). https://doi.org/10.1007/s12598-023-02306-z
63. Hydrogen in Intermetallic Compounds II. Topics in Applied Physics. 1992. https://doi.org/10.1007/3-540-54668-5.
64. Shang, S.L., Liu, Z.K.: 3 - Thermodynamic properties of magnesium alloys. In: Pekguleryuz, M.O., Kainer, K.U., Arslan Kaya, A. (eds.) Fundamentals of Magnesium Alloy Metallurgy, pp. 85–124. Woodhead Publishing (2013)
65. Stampfer, J.F., Jr., Holley, C.E., Jr., Suttle, J.F.: The magnesium-hydrogen system. J. Am. Chem. Soc. **82**(14), 3504–3508 (1960). https://doi.org/10.1021/ja01499a006
66. Flanagan, T.B., Park, C.N., Oates, W.A.: Hysteresis in solid state reactions. Prog. Solid State Chem. **23**(4), 291–363 (1995). https://doi.org/10.1016/0079-6786(95)00006-G
67. Zhu, M., Lu, Y., Ouyang, L., Wang, H.: Thermodynamic tuning of Mg-based hydrogen storage alloys: a review. Materials. **6**(10), 4654–4674 (2013). https://doi.org/10.3390/ma6104654
68. Liu, P., Lian, J., Chen, H., Liu, B., Zhou, S.: In situ formation of Mg2Ni on magnesium surface via hydrogen activation for improving hydrogen sorption performance. ACS Appl. Energy Mater. **5**(5), 6043–6049 (2022). https://doi.org/10.1021/acsaem.2c00465
69. Kudiiarov, V.N., Kenzhiyev, A., Mostovshchikov, A.V.: Improvement of the hydrogen storage characteristics of MgH(2) with Al nano-catalyst produced by the method of electric explosion of wires. Materials (2024). https://doi.org/10.3390/ma17030639
70. Luo, Q., Li, J., Li, B., Liu, B., Shao, H., Li, Q.: Kinetics in Mg-based hydrogen storage materials: enhancement and mechanism. J. Magn. Alloys. **7**(1), 58–71 (2019). https://doi.org/10.1016/j.jma.2018.12.001
71. Wang, H., Yan, H., Ren, J., Li, B., Nyamsi, S.N., Wu, Z.: Microwave plasma enhancing Mg-based hydrogen storage: thermodynamics evaluation and economic analysis of coupling SOFC for heat and power generation. Front. Therm. Eng. (2022). https://doi.org/10.3389/fther.2022.886322
72. Baran, A., Polański, M.: Magnesium-based materials for hydrogen storage-a scope review. Materials (2020). https://doi.org/10.3390/ma13183993
73. Hannappel, P., Vogt, M., Heubner, F., Balcerzak, M., Weißgärber, T.: Predicting hydrogen storage properties of multicomponent metal hydrides: modeling of pressure, capacity, hysteresis, and slope. Acta Mater. **296**, 121226 (2025). https://doi.org/10.1016/j.actamat.2025.121226
74. Pivak, Y., Schreuders, H., Dam, B.: Thermodynamic properties, hysteresis behavior and stress-strain analysis of MgH2 thin films, studied over a wide temperature range. Crystals **2**(2), 710–729 (2012)
75. Bourezg, Y.I., Azzeddine, H., Abib, K., Huang, Y., Bradai, D., Langdon, T.G.: Recrystallization in an Mg-Nd alloy processed by high-pressure torsion: a calorimetric analysis. J. Mater. Res. Technol. **9**(3), 3047–3054 (2020). https://doi.org/10.1016/j.jmrt.2020.01.035
76. Li, Z., Ding, H., Huang, Y., Langdon, T.G.: An evaluation of the mechanical properties, microstructures, and strengthening mechanisms of pure Mg processed by high-pressure torsion at different temperatures. Adv. Eng. Mater. **24**(10), 2200799 (2022). https://doi.org/10.1002/adem.202200799
77. Zhang, J., Li, Z., Wu, Y., Guo, X., Ye, J., Yuan, B., et al.: Recent advances on the thermal destabilization of Mg-based hydrogen storage materials. RSC Adv. **9**(1), 408–428 (2019). https://doi.org/10.1039/C8RA05596C

78. Zhu, Y., Ma, W., Chai, X., Gu, Y., Wu, W., Chen, H., et al.: Advances in catalysts for Magnesium-based hydrogen storage materials. Research (2025). https://doi.org/10.34133/research.1036
79. Jiang, Y., Si, N., Wang, Z., Zhang, H., Jiang, W.: Improved hydrogen storage kinetic properties of MgH2 with NiO/NiCo(Fe)2O4/(Ni). Energy Fuels **38**(24), 23804–23814 (2024). https://doi.org/10.1021/acs.energyfuels.4c04640
80. Fu, Y., Ding, Z., Ren, S., Li, X., Zhou, S., Zhang, L., et al.: Effect of in-situ formed Mg2Ni/Mg2NiH4 compounds on hydrogen storage performance of MgH2. Int. J. Hydrogen Energy **45**(52), 28154–28162 (2020). https://doi.org/10.1016/j.ijhydene.2020.03.089
81. López Gómez, E.I., Gonzalez, J., Cubero-Sesin, J.M., Huot, J.: Synthesis of nanostructured Mg2Ni for hydrogen storage by mechanical alloying via high-pressure torsion. Reactions **5**(4), 651–663 (2024). https://doi.org/10.3390/reactions5040033
82. Marzouki, M., Ghodbane, O., Abdellaoui, M.: Study of hydrogen absorption kinetics of Mg2Ni-based powders produced by high-injected shock power mechanical alloying and subsequent annealing. Mater. Renew. Sustain. Energy (2013). https://doi.org/10.1007/s40243-013-0009-y
83. Wen, J., de Rango, P., Allain, N., Novelli, M., Grosdidier, T., Laversenne, L.: In situ observation and kinetic modeling of the fundamental mechanisms underlying hydrogen sorption in forged Mg–Mg2Ni composites. Int. J. Hydrogen Energy **94**, 1160–1173 (2024). https://doi.org/10.1016/j.ijhydene.2024.11.118
84. Chen, Y., Dai, J., Song, Y.: Stability and hydrogen adsorption properties of Mg/Mg2Ni interface: a first principles study. Int. J. Hydrogen Energy **43**(34), 16598–16608 (2018). https://doi.org/10.1016/j.ijhydene.2018.07.031
85. Iturbe-García, J.L., García-Núñez, M.R., López-Muñoz, B.E.: Synthesis of the Mg2Ni alloy prepared by mechanical alloying using a high energy ball mill. J. Mexican Chem. Society. **54**(1), 964 (2010). https://doi.org/10.29356/jmcs.v54i1.964
86. Grigorova, E., Tzvetkov, P., Todorova, S., Markov, P., Spassov, T.: Facilitated synthesis of Mg2Ni based composites with attractive hydrogen sorption properties. Materials **14**(8), 1936 (2021). https://doi.org/10.3390/ma14081936
87. Jiang, H., Ding, Z., Li, Y., Lin, G., Li, S., Du, W., et al.: Hierarchical interface engineering for advanced magnesium-based hydrogen storage: synergistic effects of structural design and compositional modification. Chem. Sci. **16**(18), 7610–7636 (2025). https://doi.org/10.1039/d5sc01169h
88. Yoon, M.-S., Hur, J., Park, S.-H., Lee, U.-J., Xu, G., Park, H.-K., et al.: Role of solute elements in Mg-Mg2Ni hydrogen storage alloys: a first-principles calculation study. J. Magnesium Alloys **12**(11), 4574–4593 (2024). https://doi.org/10.1016/j.jma.2024.11.019
89. Polanski, M., Nielsen, T.K., Cerenius, Y., Bystrzycki, J., Jensen, T.R.: Synthesis and decomposition mechanisms of Mg2FeH6 studied by in-situ synchrotron X-ray diffraction and high-pressure DSC. Int. J. Hydrogen Energy **35**(8), 3578–3582 (2010). https://doi.org/10.1016/j.ijhydene.2010.01.144
90. Iosub, V., Matsunaga, T., Tange, K., Ishikiriyama, M.: Direct synthesis of Mg(AlH4)2 and CaAlH5 crystalline compounds by ball milling and their potential as hydrogen storage materials. Int. J. Hydrogen Energy **34**(2), 906–912 (2009). https://doi.org/10.1016/j.ijhydene.2008.11.013
91. Gao, M., Zhao, S., Yang, H., Wu, X., Xiao, Y.: An analysis of the influence of DSC parameters on the measurement of the thermal properties of phase-change material. Materials **17**(23), 5689 (2024). https://doi.org/10.3390/ma17235689